AGU ADVANCING EARTH AND SPACE SCIENCE

JGR Atmospheres

RESEARCH ARTICLE
10.1029/2022JD037822

Optimizing the Isoprene Emission Model MEGAN With Satellite and Ground-Based Observational Constraints

Christian A. DiMaria[1], Dylan B. A. Jones[1], Helen Worden[2], A. Anthony Bloom[3], Kevin Bowman[3], Trissevgeni Stavrakou[4], Kazuyuki Miyazaki[3], John Worden[3], Alex Guenther[5], Chinmoy Sarkar[5], Roger Seco[6], Jeong-Hoo Park[7], Julio Tota[8], Eliane Gomes Alves[9], and Valerio Ferracci[10]

[1]Department of Physics, University of Toronto, Toronto, ON, Canada, [2]Atmospheric Chemistry Observations & Modeling Laboratory, National Center for Atmospheric Research, Boulder, CO, USA, [3]Jet Propulsion Laboratory, California Institute of Technology, Pasadena, CA, USA, [4]Royal Belgian Institute for Space Aeronomy (BIRA-IASB), Brussels, Belgium, [5]Department of Earth System Science, University of California, Irvine, CA, USA, [6]Institute of Environmental Assessment and Water Research (IDAEA-CSIC), Barcelona, Spain, [7]Air Quality Research Division, National Institute of Environmental Research, Incheon, Republic of Korea, [8]Julio Tota, Instituto de engenharia e Geociências, Universidade Federal do Oeste do Pará, UFOPA, Santarém, Brazil, [9]Department of Biogeochemical Processes, Max Planck Institute for Biogeochemistry, Jena, Germany, [10]School of Water, Energy and Environment, Cranfield University, Cranfield, UK

Key Points:

- Satellite and ground based observations were used to optimize an isoprene emission model in a Bayesian model-data fusion framework
- Optimization with satellite-based emissions was highly uncertain due to observation biases and a high sensitivity to model input errors
- Ground-based observations showed that Amazonian isoprene emissions were 5× more sensitive to temperature than UK isoprene emissions

Supporting Information:

Supporting Information may be found in the online version of this article.

Correspondence to:

C. A. DiMaria,
christian.dimaria@mail.utoronto.ca

Citation:

DiMaria, C. A., Jones, D. B. A., Worden, H., Bloom, A. A., Bowman, K., Stavrakou, T., et al. (2023). Optimizing the isoprene emission model MEGAN with satellite and ground-based observational constraints. *Journal of Geophysical Research: Atmospheres*, *128*, e2022JD037822. https://doi.org/10.1029/2022JD037822

Received 8 SEP 2022
Accepted 26 JAN 2023

Author Contributions:

Conceptualization: Christian A. DiMaria, Dylan B. A. Jones, Helen Worden, A. Anthony Bloom, Kevin Bowman, Kazuyuki Miyazaki, John Worden, Alex Guenther
Formal analysis: Christian A. DiMaria
Investigation: Christian A. DiMaria
Methodology: Christian A. DiMaria, Dylan B. A. Jones, Helen Worden, A. Anthony Bloom, Kevin Bowman, Trissevgeni Stavrakou, Kazuyuki Miyazaki, John Worden, Roger Seco, Valerio Ferracci

Abstract Isoprene is a hydrocarbon emitted in large quantities by terrestrial vegetation. It is a precursor to several air quality and climate pollutants including ozone. Emission rates vary with plant species and environmental conditions. This variability can be modeled using the Model of Emissions of Gases and Aerosols from Nature (MEGAN). MEGAN parameterizes isoprene emission rates as a vegetation-specific standard rate which is modulated by scaling factors that depend on meteorological and environmental driving variables. Recent experiments have identified large uncertainties in the MEGAN temperature response parameterization, while the emission rates under standard conditions are poorly constrained in some regions due to a lack of representative measurements and uncertainties in landcover. In this study, we use Bayesian model-data fusion to optimize the MEGAN temperature response and standard emission rates using satellite- and ground-based observational constraints. Optimization of the standard emission rate with satellite constraints reduced model biases but was highly sensitive to model input errors and drought stress and was found to be inconsistent with ground-based constraints at an Amazonian field site, reflecting large uncertainties in the satellite-based emissions. Optimization of the temperature response with ground-based constraints increased the temperature sensitivity of the model by a factor of five at an Amazonian field site but had no impact at a UK field site, demonstrating significant ecosystem-dependent variability of the isoprene emission temperature sensitivity. Ground-based measurements of isoprene across a wide range of ecosystems will be key for obtaining an accurate representation of isoprene emission temperature sensitivity in global biogeochemical models.

Plain Language Summary Plants emit a reactive gas called isoprene which has a large impact on air quality and climate throughout the world. This impact can be studied and quantified using computer models, but there are large uncertainties in modeled isoprene emission rates. There are few measurements to constrain the emission rates of many vegetation species. There are also uncertainties in the relationship between isoprene emissions and temperature, which makes it difficult to predict how air quality may change in a warming climate. Our goal in this study was to reduce uncertainties in a widely-used isoprene emission model by constraining the model with observations. We used satellite observations to constrain the emission rates in a diverse range of ecosystems, but these results were sensitive to many different sources of error including drought stress. Using ground-based observations, we found that isoprene emissions were five times more sensitive to temperature at a measurement site in the Amazon rainforest than they were at a UK measurement site. Updating the temperature sensitivity of isoprene emission models has the potential to improve models of air quality during extreme heat events and in a warming climate.

1. Introduction

Isoprene is a reactive volatile organic compound (VOC) emitted by terrestrial vegetation, possibly contributing to abiotic stress tolerance (Monson et al., 2021). Annual isoprene emissions exceed all other non-methane VOCs,

Resources: Trissevgeni Stavrakou, Alex Guenther, Chinmoy Sarkar, Roger Seco, Jeong-Hoo Park, Julio Tota, Eliane Gomes Alves, Valerio Ferracci
Software: Christian A. DiMaria, A. Anthony Bloom
Supervision: Dylan B. A. Jones
Validation: Trissevgeni Stavrakou
Visualization: Christian A. DiMaria
Writing – original draft: Christian A. DiMaria
Writing – review & editing: Christian A. DiMaria, Dylan B. A. Jones, Helen Worden, A. Anthony Bloom, Kevin Bowman, Trissevgeni Stavrakou, Kazuyuki Miyazaki, John Worden, Alex Guenther, Chinmoy Sarkar, Roger Seco, Jeong-Hoo Park, Julio Tota, Eliane Gomes Alves, Valerio Ferracci

with an estimated global emission rate of 360–800 Tg yr^{-1} (Guenther et al., 2012). Emissions vary widely among plant species and are concentrated in tropical terrestrial ecosystems (Guenther et al., 1995, 2006), but can also be significant in temperate regions during the growing season (Potosnak et al., 2014; Seco et al., 2015; Wiedinmyer et al., 2005). Emission rates vary in response to temperature and sunlight (Guenther et al., 1993), and are modulated on seasonal and interannual timescales by landcover and canopy environment changes (Alves et al., 2016; Chen et al., 2018) as well as environmental stressors such as drought (X. Jiang et al., 2018; Potosnak et al., 2014; Seco et al., 2015) and CO_2 inhibition (Heald et al., 2009).

Isoprene has a short atmospheric lifetime on the order of hours due to rapid oxidation by the hydroxyl (OH) radical (Sprengnether et al., 2002). This oxidation contributes to the formation of air quality and climate pollutants, including ozone (Trainer et al., 1987), secondary organic aerosol (Claeys et al., 2004), and carbon monoxide (CO) (Z. Jiang et al., 2017). The biogenic CO source from isoprene oxidation exceeds anthropogenic and biomass burning emissions in many regions (Hudman et al., 2008; Worden et al., 2019), and the relative contribution of biogenic CO to the total atmospheric CO burden may be increasing due to declining anthropogenic emissions (Buchholz et al., 2021; Worden et al., 2013). Isoprene is a major sink for OH, which influences the lifetime of methane and other trace gases (Karl et al., 2007, 2013). Quantifying these atmospheric chemistry impacts requires accurate isoprene emission estimates.

The Model of Emissions of Gases and Aerosols from Nature (MEGAN) is widely used to estimate isoprene emissions (Guenther et al., 2006, 2012). In MEGAN, isoprene emissions are the product of a vegetation-specific standard emission rate and dimensionless scaling functions which depend on temperature, sunlight, leaf area index (LAI), leaf age, and soil moisture (SM). MEGAN isoprene emissions are highly sensitive to meteorology and landcover (Arneth et al., 2011; Misztal et al., 2016) and are thus dependent on the accuracy and resolution of these model inputs (Ashworth et al., 2010; Pugh et al., 2013). Model performance is generally good when accurate driving variables are used (Situ et al., 2014; see also Filella et al., 2018; Sarkar et al., 2020), but significant sources of uncertainty remain. These include the empirical parameterization of the standard emission rates and the dimensionless scaling functions, particularly the temperature and drought stress responses (Angot et al., 2020; Guenther et al., 2006; X. Jiang et al., 2018; Kramshøj et al., 2016; Potosnak et al., 2014; Seco et al., 2015, 2020, 2022).

The standard emission rates are based on leaf- or canopy-scale isoprene flux measurements which can be extrapolated globally over regions with similar landcover (Guenther et al., 1995). This methodology introduces biases due to the large variability of isoprene emission rates among plant species (Guenther et al., 1993) and within ecosystems (Batista et al., 2019; Li et al., 2021). Emission rate biases are exacerbated by landcover uncertainties (Opacka et al., 2021), particularly in tropical regions (Fang et al., 2013; Gu et al., 2017; Mougin et al., 2019). An additional source of uncertainty is the relative lack of isoprene flux measurements to constrain emission rates in the tropics (Guenther et al., 2006; Marais et al., 2014). Constraining the standard emission rates using satellite observations of the isoprene oxidation product formaldehyde has been shown to reduce emission biases in MEGAN (Marais et al., 2014), allowing the model to be improved in regions where ground-based isoprene flux measurements are unavailable.

MEGAN's temperature response algorithm, which simulates the exponential increase in emissions with temperature up to an optimum value (Guenther et al., 1993, 1995), is another source of uncertainty. Recent experiments with Arctic vegetation (Angot et al., 2020; Kramshøj et al., 2016; Seco et al., 2020, 2022) and Australian *eucalypt* trees (Emmerson et al., 2020) have found that MEGAN significantly underestimates isoprene emissions from these species at high temperatures. Updating the parameterization of the temperature response with species-specific measurements in Australia has been shown to improve MEGAN isoprene emissions estimates, with significant consequences for predictions of future ozone pollution in a warming climate (Emmerson et al., 2020). Because temperature and sunlight are the primary drivers of short-term isoprene emission variability (Guenther et al., 1993), uncertainties in the MEGAN temperature response have significant implications for isoprene emission modeling.

In this study we use Bayesian model-data fusion, a form of data assimilation which combines information from models and observations in a statistically rigorous way, to optimize the parameterization of the MEGAN standard emission rate and temperature response. Using top-down isoprene emissions based on satellite formaldehyde retrievals from the Ozone Monitoring Instrument (OMI; Bauwens et al., 2016) and the TROPOspheric Monitoring Instrument (TROPOMI), we constrain the standard emission rate in several regions to reduce model

biases. Eddy covariance isoprene measurements at the BR-Sa1 AmeriFlux site in the Tapajós National Forest in the Brazilian Amazon and isoprene atmospheric mixing ratio measurements at Wytham Woods near Oxford, United Kingdom, are used to constrain the temperature response parameterization independently in two distinct ecosystems. The sensitivity of our optimization to model input errors and drought stress, discrepancies between satellite- and ground-based constraints, and the variability of the temperature response between the two field sites are discussed.

2. Methods and Data

In Section 2.1 we describe MEGAN, with a particular focus on the model sensitivity to temperature. Section 2.2 introduces the ground-based isoprene measurements (Section 2.2.1) and satellite-based top-down isoprene flux estimates (Section 2.2.2). Finally, Section 2.3 describes the Bayesian model-data fusion and validates the method with a simulated observation experiment.

2.1. MEGAN and the Temperature Activity Factor γ_T

MEGAN is an empirical model in which isoprene emissions are the product of a vegetation-specific standard rate and activity factors (i.e., dimensionless scaling functions) (Guenther et al., 2006) which depend on meteorology, leaf phenology, and environmental conditions (Guenther et al., 1991, 1993). This is shown in the following equation:

$$E_{\mathrm{ISOP}} = E_0 \times C_{\mathrm{CE}} \times \gamma_T \times \gamma_{\mathrm{PAR}} \times \gamma_{\mathrm{LAI}} \times \gamma_{\mathrm{AGE}} \times \gamma_{\mathrm{CO_2}} \times \gamma_{\mathrm{SM}}, \quad (1)$$

where E_{ISOP} is the isoprene emission rate, E_0 is the standard emission rate, and γ_{T}, γ_{PAR}, γ_{LAI}, γ_{AGE}, $\gamma_{\mathrm{CO_2}}$, and γ_{SM} are activity factors that represent the emission sensitivity to temperature (T), photosynthetically active radiation (PAR), LAI, leaf age, CO_2 partial pressure, and SM stress respectively (Guenther et al., 2006, 2012). Diurnal variability of modeled emissions is controlled by temperature and sunlight, whereas longer term variability is influenced by changes in leaf phenology, landcover, drought stress, and CO_2 inhibition (Alves et al., 2016; Chen et al., 2018; Guenther et al., 1993; Heald et al., 2009; X. Jiang et al., 2018; Opacka et al., 2021). C_{CE} is a normalization constant which ensures that $E_{\mathrm{ISOP}} = E_0$ under standard conditions (see Text S1 in Supporting Information S1).

We use the Parameterized Canopy Environment Emission Activity (PCEEA) algorithm for the activity factors γ_{T}, γ_{PAR}, and γ_{LAI} and the empirical parameter values contained therein (Guenther et al., 2006). In particular, the temperature response function γ_{T} is given by

$$\gamma_T = E_{\mathrm{Opt}} \left[\frac{C_{T2} \times \exp(C_{T1} \times x)}{(C_{T2} - C_{T1} \times (1 - \exp(C_{T2} \times x)))} \right], \quad (2)$$

where C_{T1} (80 kJ mol^{-1}) and C_{T2} (200 kJ mol^{-1}) are fitting parameters, x is a temperature dependent variable given by

$$x = \left[\frac{\frac{1}{T_{\mathrm{Opt}}} - \frac{1}{T}}{R} \right], \quad (3)$$

where T is the air temperature (K) (assumed to be equal to the leaf temperature in the PCEEA algorithm) and R is the ideal gas constant (0.00831 kJ K^{-1} mol^{-1}). Equation 2 is based on a photosynthetic electron transport model in which activity increases with temperature up to an optimum value (Guenther et al., 1991). E_{Opt} is an empirical parameter given by the equation

$$E_{\mathrm{Opt}} = C_{\mathrm{EO}} \times \exp\left(K_2 \left(T_{\mathrm{daily}} - 297\right)\right), \quad (4)$$

where C_{E0} (1.75) and K_2 (0.08) are empirical coefficients and T_{daily} is the average air temperature of the past 24 hr (Guenther et al., 2006). T_{Opt} is an empirical parameter defined as follows:

$$T_{\mathrm{Opt}} = T_{\mathrm{Max}} + \left(K_1 \left(T_{\mathrm{daily}} - 297\right)\right), \quad (5)$$

where T_{Max} (313 K) is the peak emission temperature under standard conditions and K_1 (0.6) is an empirical coefficient. Equations 4 and 5 describe how the peak isoprene emission rate, as well as the temperature at which it occurs, changes as a function of T_{daily} (see Text S2 in Supporting Information S1). This hysteresis, or long-term temperature response, is based on a small number of experiments and is highly uncertain (Geron et al., 2000; Hanson & Sharkey, 2001; Monson et al., 1994; Pétron et al., 2001).

We quantify the sensitivity of γ_T to temperature using the Q_{10} metric, which is defined as γ_T at 313 K divided by γ_T at 303 K (Seco et al., 2020). All Q_{10} values presented in this study are calculated using Equations 2–5 with an assumed T_{daily} of 297 K. This ensures that changes in Q_{10} can be entirely attributed to changes in the γ_T parameters rather than ambient temperature, allowing for a direct comparison of this metric between measurement sites with different environmental conditions.

Unless otherwise stated, we drive MEGAN2.1 (Guenther et al., 2012) with hourly meteorology fields from the Modern-Era Retrospective analysis for Research and Applications, Version 2 (MERRA-2; Gelaro et al., 2017) at 0.5° × 0.625° spatial resolution and 8-day average LAI at 2° × 2.5° resolution from the Moderate Resolution Imaging Spectroradiometer (MODIS) aboard NASA's Terra and Aqua satellites (Yuan et al., 2011, 2020). Local temperature measurements are used to drive the model at BR-Sa1 (Sarkar et al., 2020, 2022) and Wytham Woods (Ferracci, Bolas, et al., 2020, Ferracci, Harris, et al., 2020) instead of MERRA-2 temperature data. We used hourly Goddard Earth Observing System-Forward Processing (GEOS-FP; provided by the Global Modeling and Assimilation Office (GMAO) at NASA Goddard Space Flight Center) PAR and windspeed data to filter the Wytham Woods observations due to their higher native resolution (0.25° × 0.3125°) relative to MERRA-2. We used gridded $\boldsymbol{\gamma}_{SM}$ values at 0.5° × 0.5° from 2005–2015 as obtained with Community Land Model (CLM) 4.5 and the MEGAN3 SM algorithm (X. Jiang et al., 2018). There are large uncertainties associated with the drought stress response $\boldsymbol{\gamma}_{SM}$ (X. Jiang et al., 2018; Potosnak et al., 2014; Seco et al., 2015; Opacka et al., 2022). To quantify the sensitivity of our analysis to this model component, we run our E_0 optimization experiments both with and without $\boldsymbol{\gamma}_{SM}$ enabled. We fix $\gamma_{CO_2} = 1$ due to the insignificance of CO_2 inhibition on short timescales (Heald et al., 2009). A priori E_0 at 0.25° × 0.3125° spatial resolution are based on the CLM plant functional type distribution (Lawrence et al., 2011).

2.2. Data

2.2.1. Eddy Covariance and Atmospheric Mixing Ratio Measurements

Isoprene emissions can be estimated from tower- or aircraft-based eddy covariance measurements (Guenther & Hills., 1998; Karl et al., 2009). This approach is useful for constraining the diurnal variability of isoprene emissions, making it well-suited for characterizing the temperature response (Misztal et al., 2014; Seco et al., 2015, 2022; Yu et al., 2017). In this study, we use tower-based eddy covariance isoprene flux measurements from the AmeriFlux site BR-Sa1 in Brazil's Tapajós National Forest (2.86°S, 54.96°W) (Sarkar et al., 2020, 2022), as well as isoprene mixing ratio measurements from the 2018 Wytham Isoprene iDirac Oak Tree Measurements (WIsDOM) campaign in Wytham Woods near Oxford, UK (51.46°N, 1.20°W) (Ferracci, Bolas, et al., 2020, Ferracci, Harris, et al., 2020). The locations of these field sites are shown in Figure 1. The field sites were selected to represent contrasting ecosystems based on the availability of concurrent isoprene and temperature measurements. Tapajós National Forest is a protected Amazonian old-growth closed-canopy evergreen tropical forest (Sarkar et al., 2020), while the Wytham Woods site is a mixed temperate woodland where *Quercus robur* (European oak) is the dominant isoprene emitter (Butt et al., 2009).

The BR-Sa1 data set consists of hourly isoprene emission measurements and surface air temperature measurements from 1 to 16 June 2014 (Sarkar et al., 2020, 2022). The isoprene fluxes were calculated from proton transfer reaction time-of-flight mass spectrometry (PTR-TOF-MS) isoprene mixing ratio measurements using eddy covariance techniques. The spatiotemporal overlap of the BR-Sa1 data with the OMI-based GlobEmission data allows for a direct comparison of top-down and eddy covariance constraints. Uncertainties were estimated to be 15%, based on measurement errors and the variability of the observations (Sarkar et al., 2020). MEGAN was driven with locally measured temperature data at this site. The SM response $\boldsymbol{\gamma}_{SM}$ was equal to 1 at BR-Sa1 throughout the study period (X. Jiang et al., 2018). Further details about the BR-Sa1 measurements, as well as a more detailed site description, are available in Sarkar et al. (2020).

The WIsDOM data set used in this study consists of isoprene mixing ratio and temperature measurements taken at a height of 15.55 m above ground level in a UK mixed forest canopy from 25 May to 6 November 2018 (Ferracci,

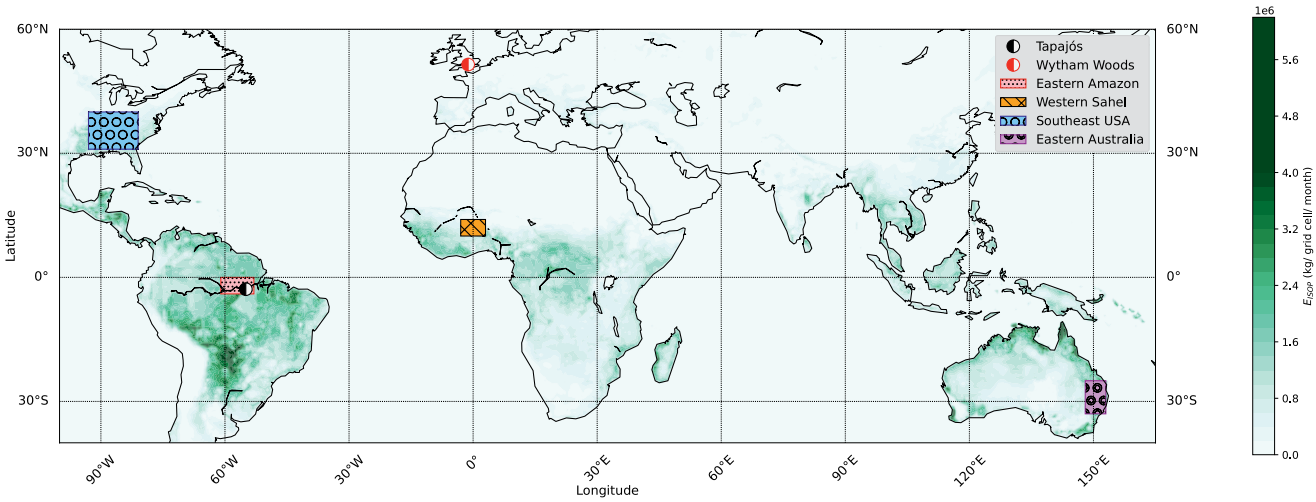

Figure 1. Locations of the 4 study regions used for the optimization of E_0 with top-down constraints (rectangles) and the two field sites used for the optimization of γ_T with eddy covariance and mixing ratio constraints (circles). The colorbar represents the mean isoprene emission rate (kg/0.5° × 0.5° grid° cell/month) from the Ozone Monitoring Instrument-based GlobEmission top-down isoprene emission data set from 2005 to 2014.

Bolas, et al., 2020, Ferracci, Harris, et al., 2020). Isoprene mixing ratios were measured using the iDirac (Bolas et al., 2020) portable gas chromatograph with photo-ionization detection with a measurement precision of 10% and a time resolution of 20 min. Temperature was measured with an EasyLog probe (EL-USB-2, Lascard Ltd.) placed next to the iDirac inlet; this temperature data set was used to drive MEGAN at this site. A long and uninterrupted heatwave occurred at Wytham Woods from 22 June to 8 August 2018 and the associated drought had a significant impact on local isoprene emission rates (Ferracci, Bolas, et al., 2020; Otu-Larbi et al., 2020). To avoid the impact of drought stress we use only the data from 25 May to 21 June, hereafter referred to as the preheatwave period. Local PAR measurements were not available at Wytham Woods during the preheatwave period, so we used hourly GEOS-FP PAR at 0.25° × 0.325° resolution to drive MEGAN. Following Ferracci, Bolas, et al. (2020), we used a linear mapping to account for any systematic offset between the GEOS-FP PAR and the locally measured PAR which was available at Wytham Woods in September 2018 (see Text S4 in Supporting Information S1). Additionally, hourly GEOS-FP 10-m wind speed and planetary boundary layer height were used for data filtering (see Section 3.3.2). Wytham Woods data are available for download at https://archive.ceda.ac.uk (Ferracci, Harris, et al., 2020). Further details about the WIsDOM campaign are available in Ferracci, Bolas, et al. (2020).

2.2.2. Top-Down Emissions

Isoprene emissions can be estimated from satellite retrievals of its high-yield oxidation product formaldehyde (CH_2O) (Palmer et al., 2003). Regional and global estimates have been obtained from several sensors including the Global Ozone Monitoring Experiment (GOME) (Palmer et al., 2003), the SCanning Imaging Absorption SpectroMeter for Atmospheric CHartographY (SCIAMACHY) (Barkley et al., 2013; Stavrakou et al., 2009c), GOME-2 (Stavrakou et al., 2015), the OMI (Bauwens et al., 2016; Kaiser et al., 2018; Marais et al., 2012), and the TROPOMI. Here we use top-down isoprene estimates from (a) the GlobEmission global data set (2005–2014) constrained by OMI CH_2O columns (Bauwens et al., 2016), and (b) the SOLFEO regional data set over South America constrained by TROPOMI CH_2O columns in 2018.

The 10-year (2005–2014) GlobEmission inventory (Bauwens et al., 2016) was created by assimilating OMI CH_2O column retrievals into the IMAGESv2 chemistry-transport model (Müller & Stavrakou, 2005; Stavrakou, Müller, De Smedt, Van Roozendael, Kanakidou et al., 2009, Stavrakou et al., 2009b) using an adjoint-based variational data assimilation scheme. The inversion is performed at a spatial resolution of 2° × 2.5° on a monthly basis. The top-down emissions are further downscaled to a daily inventory resolution at 0.5° × 0.5°, based on the spatiotemporal variability of the a priori MEGAN inventory used in the inversions. We use the GlobEmission data in the Eastern Amazon basin (0°S–4°S, 53°W–61°W), the Western Sahel (10°N–14°N, 3°W–3°E), the Southeastern United States (31°N–40°N, 81°W–93°W), and Eastern Australia (25°S–33°S, 148°E–153°E). Data for the year 2005 was omitted from our analysis due to missing MEGAN driving variables. Figure 1 shows

the mean GlobEmission isoprene emissions, with the locations of the study regions indicated. Discrepancies between MEGAN and top-down flux estimates have been previously documented in each of these regions (Bauwens et al., 2016; Marais et al., 2014; Worden et al., 2019), with the Amazon and Southeast USA accounting for a significant portion of the total global annual isoprene emissions (Guenther et al., 2006). The SOLFEO data set (https://emissions.aeronomie.be/index.php/tropomi-based/isoprene-sa) provided an independent set of top-down constraints for the E_0 optimization in the Eastern Amazon region. This data set provides monthly average isoprene emission rate estimates for 2018 at $0.5° \times 0.5°$ resolution in South America, based on an assimilation of TROPOMI CH_2O observations into the regional chemistry-transport model MAGRITTEv1.1 (Müller et al., 2019; Stavrakou et al., 2016). Both top-down emission data sets are publicly available from the Emission portal at https://emissions.aeronomie.be/.

A validation study using a network of ground-based remotely-sensed CH_2O columns revealed a substantial bias in the TROPOMI CH_2O columns (De Smedt et al., 2021; Vigouroux et al., 2020). The estimated bias is found to be low for high columns (−30% for values higher than 8×10^{15} mole cm^{-2}) and high for low columns (+26% for values lower than 2.5×10^{15} mole cm^{-2}). Based on those comparisons, bias-corrected TROPOMI columns are given by the linear regression relationship: $1.56 \times C – 1.72 \times 10^{15}$ mole cm^{-2}, where C is the TROPOMI CH_2O column (in mole cm^{-2}). The adjustment increases the columns by 20%–50% for TROPOMI columns within $(5–40) \times 10^{15}$ mole cm^{-2}. Those higher columns would entail substantially higher top-down isoprene fluxes than those derived based on the standard TROPOMI product. Since the OMI and TROPOMI formaldehyde products were retrieved using similar algorithms (De Smedt et al., 2018), the top-down estimates of the GlobEmission data set are also likely similarly underestimated.

The optimization of E_0 was found to be largely insensitive to the assumed uncertainty of the top-down emissions (see Text S3 in Supporting Information S1). An uncertainty of 30% was used for consistency with the biases revealed by ground-based validation studies described above, but this is likely an underestimate of the true uncertainty in some regions (De Smedt et al., 2021; Vigouroux et al., 2020).

2.3. Parameter Estimation Using Bayesian Model-Data Fusion

We use Bayesian model-data fusion, a form of data assimilation used to combine information from models and observations in a statistically rigorous way, to constrain the MEGAN parameters with observations. Given a parameter vector $\boldsymbol{x}$ and observations $\boldsymbol{O}$, we can derive the posterior probability density function of $\boldsymbol{x}$ as

$$P(\boldsymbol{x}|\boldsymbol{O}) \propto P(\boldsymbol{x})P(\boldsymbol{O}|\boldsymbol{x}) \tag{6}$$

where $P(\boldsymbol{x})$ is the a priori probability distribution of $\boldsymbol{x}$ and $P(\boldsymbol{O}|\boldsymbol{x})$ is the observation probability given $\boldsymbol{x}$, also called the model likelihood function. In this study we assume a non-informative uniform $P(\boldsymbol{x})$ for all parameters such that $P(x) = 1$ for all $\boldsymbol{x} \in [\boldsymbol{x}_{\min}, \boldsymbol{x}_{\max}]$ and $P(x) = 0$ outside of this range. The limits $\boldsymbol{x}_{\min}$ and $\boldsymbol{x}_{\max}$ were respectively set to 1/5 and 5 times the a priori parameter value for all parameters except for T_{Max}, which was constrained to $T_{\text{Max}} \in [20°C, 60°C]$ to avoid unphysical parameterizations. For all $\boldsymbol{x} \in [\boldsymbol{x}_{\min}, \boldsymbol{x}_{\max}]$ the posterior probability $P(\boldsymbol{x}|\boldsymbol{O})$ is then proportional to the observation probability $P(\boldsymbol{O}|\boldsymbol{x})$, which we define for N observations as

$$P(\boldsymbol{O}|\boldsymbol{x}) = \exp\left(-0.5 \sum_{n=1}^{N} \frac{(M_n - O_n)^2}{\sigma_n^2}\right) \tag{7}$$

where O_n is the nth observation (top-down or eddy covariance isoprene measurements), M_n is the corresponding model state (in our case, MEGAN isoprene emissions), and σ_n^2 is the observation error variance. This definition of $P(\boldsymbol{O}|\boldsymbol{x})$ assumes Gaussian error statistics and no covariance between observation errors.

We sample the probability distribution $P(\boldsymbol{x}|\boldsymbol{O})$ using an adaptive Metropolis-Hastings Markov Chain Monte Carlo (MHMCMC) algorithm (Haario et al., 2001). The MHMCMC algorithm has been previously applied to parameter estimation problems in the context of ecosystem modeling (Bloom & Williams, 2015; Bloom et al., 2015; Xu et al., 2006; Ziehn et al., 2012), and consists of the following 4 basic steps:

1. Choose an initial parameter state vector: $\boldsymbol{x_i}$
2. Perturb the parameters: $\boldsymbol{x}_{i+1} = \boldsymbol{x}_i + \Delta\boldsymbol{x}$
3. Run model with both sets of parameters: $\boldsymbol{M}(\boldsymbol{x}_i)$ and $\boldsymbol{M}(\boldsymbol{x}_{i+1})$
4. Accept new parameters if $\frac{P(\boldsymbol{x}_{i+1}|\boldsymbol{O})}{P(\boldsymbol{x}_i|\boldsymbol{O})} > U \in [0, 1]$; else $\boldsymbol{x}_{i+1} = \boldsymbol{x}_i$

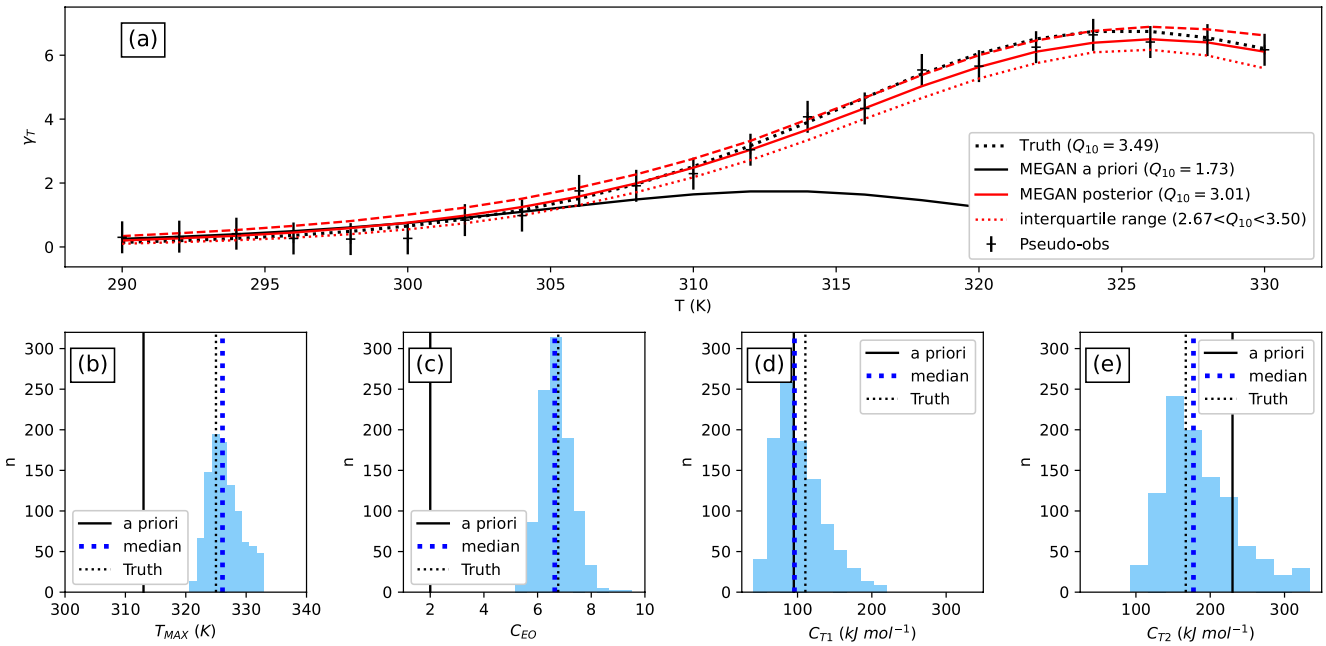

Figure 2. (a) A priori Model of Emissions of Gases and Aerosols from Nature γ_T (black), median posterior γ_T (solid red) and interquartile range (dashed red) as a function of temperature compared with pseudo-observations. The dotted black line represents the "true" γ_T as calculated using the posterior parameterization of Emmerson et al. (2020). All γ_T curves in (a) were calculated using Equation 2. The posterior parameter distributions for T_{Max}, C_{EO}, C_{T1}, and C_{T2} (from Equations 2, 4, and 5) are shown in (b–e) respectively, with the median values (dotted blue line) agreeing closely with the "true" values (thin dotted black line). The a priori parameter values are indicated by the solid black lines. The a priori probability distribution for each parameter (not shown) was uniform and spanned from 1/5 to 5 times the a priori values, except for T_{Max} which was constrained between 293 and 333 K.

In Steps 1–4, x_i is the ith iteration of the parameter state vector, $\Delta\boldsymbol{x}$ is the parameter perturbation step-size, U is a uniform distribution (Ziehn et al., 2012; see also Bloom & Williams, 2015), and $P(\boldsymbol{x}|\boldsymbol{O})$ is the observation probability, given by Equation 7 for all $\boldsymbol{x} \in [\boldsymbol{x}_{min}, \boldsymbol{x}_{max}]$ and equal to 0 otherwise. Our implementation of the MHMCMC algorithm follows Bloom et al. (2020) and uses a Matlab code developed by Yang et al. (2021, 2022).

Step 4 of the MHMCMC algorithm ensures that parameter values which maximize the probability in Equation 7 are more likely to be accepted. Because only the ratio of probabilities is used, $P(\boldsymbol{x}|\boldsymbol{O})$ does not need to be normalized. In our experiments, Steps 1–4 were repeated for 4×10^4 iterations. Following Ziehn et al. (2012), the perturbation step size Δx is adjusted every 50 iterations to achieve a parameter acceptance rate between 23% and 44%, which ensures proper sampling of the parameter space while also minimizing the required number of model iterations. The first half of the samples were then discarded, and the remaining half were subsampled by a factor of 20 to reduce correlations between samples (Ziehn et al., 2012), giving a final distribution of 1,000 parameter samples for each experiment.

We validated our MHMCMC approach using a series of simulated observation experiments. The purpose of these experiments was to ensure that the MHMCMC scheme was capable of estimating MEGAN parameters when provided with suitable observational constraints. In the initial experiment, the posterior γ_T parameterization of Emmerson et al. (2020) (based on *eucalypt* measurements) was used to calculate a "true" temperature response with Equation 2. We sampled this "true" temperature response from 290 to 330 K at 2 K intervals to produce pseudo-observations, which were perturbed with Gaussian noise (σ = 0.1–2.0, approximately 3%–60% of the mean "true" γ_T) to simulate measurement error. The PCEEA parameterization of γ_T was used as the a priori, as in all other experiments in this study. Figure 2a shows the results of a simulated observation temperature optimization experiment, with σ = 0.5. The optimized posterior γ_T is in good agreement with the truth and is much more sensitive to temperature (Q_{10} = 3.01) than the a priori (Q_{10} = 1.73). The MEGAN γ_T parameters T_{Max}, C_{EO}, C_{T1}, and C_{T2} could be constrained with pseudo-observations provided that the observation errors were sufficiently small. Figures 2b–2e show that the optimized parameters are consistent with those derived by Emmerson et al. (2020). These results demonstrate that MHMCMC is a suitable method for constraining MEGAN parameters with observations.

Additional simulated observation experiments were used to assess the impact of observation errors and temporal resolution on the optimization using time series pseudo-observations. We found that while the standard emission rate E_0 could be easily constrained with relatively imprecise (<50% error) or infrequent (e.g., monthly) observations (see Text S3 in Supporting Information S1), the γ_T parameters could only be properly constrained with more precise and higher frequency observations (see Text S5 in Supporting Information S1). No combination of γ_T parameters could be reliably constrained when observation errors exceeded 20%; some combinations required much more precise observations, while all combinations were easier to constrain at higher ambient temperatures (see Text S6 in Supporting Information S1). We therefore use 20% as a lower limit on the observation precision required to constrain γ_T, with the understanding that this may be insufficient for some parameter combinations under some ambient conditions. Given the stricter observation precision requirements, we limit our γ_T parameter optimization to the BR-Sa1 and Wytham Woods sites where we have sufficiently precise observations available. The optimization of γ_T is performed independently at each field site, and the results are compared to assess model performance in two distinct ecosystems.

3. Results

Section 3.1 presents the optimization of the standard emission rate E_0 using satellite-based top-down constraints in our four study regions (Section 3.1.1) and using eddy covariance measurements at the Amazonian BR-Sa1 site (Section 3.1.2). Section 3.2 presents the optimization of the γ_T parameters using eddy covariance observations at BR-Sa1 Section 3.2.1 and using isoprene mixing ratio measurements at the UK Wytham Woods site (Section 3.2.2).

3.1. Optimization of Standard Emission Rate E_0

3.1.1. Top-Down Constraints

Monthly OMI-based GlobEmission data were used to constrain the standard emission rate E_0 in four study regions (Figure 1) for the period of 2006–2014. The study regions were selected to represent a diversity of ecosystems with substantial isoprene emissions. The MEGAN a priori emissions were calculated as described in Section 2.1. We performed the optimization both with and without the MEGAN3 SM response γ_{SM} enabled to assess the impact of this uncertain model component. All MEGAN γ factor parameters were fixed to their a priori PCEEA values, as defined in Section 2.1.

Optimization of the standard emission rate E_0 reduced MEGAN isoprene emissions in all four study regions, leading to better agreement between MEGAN and the OMI-based GlobEmission flux estimates (Figure 3). The box-and-whisker plot in Figure 4 shows that the optimized E_0 values were well-constrained and significantly reduced relative to their a priori values. Constraining E_0 with the TROPOMI-based SOLFEO fluxes produced a consistent result in the Eastern Amazon (Figure 4), indicating that the biases observed in this region are not unique to the GlobEmission data set. Our results are consistent with previous studies which have used top-down constraints to reduce biases in modeled isoprene emissions (Kaiser et al., 2018) and in E_0 (Marais et al., 2014).

Enabling γ_{SM} reduces the a priori emissions in each region (Figure 3). The optimized E_0 values are consequently larger than in the no-γ_{SM} case (Figure 4) because some of the bias between MEGAN and GlobEmission has already been accounted for by γ_{SM}. This change was most significant in Eastern Australia, where the difference between the two optimization results is over 40% due to the large impact of γ_{SM} on the a priori emissions. The significance of drought stress for Eastern Australian isoprene emissions has been previously reported (Emmerson et al., 2019) and our results are consistent with this. Although the impact on the a priori emissions and posterior E_0 was large, inclusion of γ_{SM} had little impact on the posterior emissions in all four regions. This is an example of equifinality, in which different combinations of model inputs and parameters (in this case E_0 and γ_{SM}) produce the same output. This is a major source of uncertainty in top-down emission optimizations due to the risk of misattributing errors in other model components to biases in E_0, which in principle allows us to obtain improved emissions estimates while using incorrect modeling assumptions. We discuss this in the context of the drought stress factor γ_{SM} in Section 4.1.

3.1.2. Eddy Covariance Constraints

The standard emission rate E_0 was constrained using hourly eddy covariance measurements at the BR-Sa1 site. For this experiment, MEGAN was driven with locally measured air temperature data. The a priori MEGAN

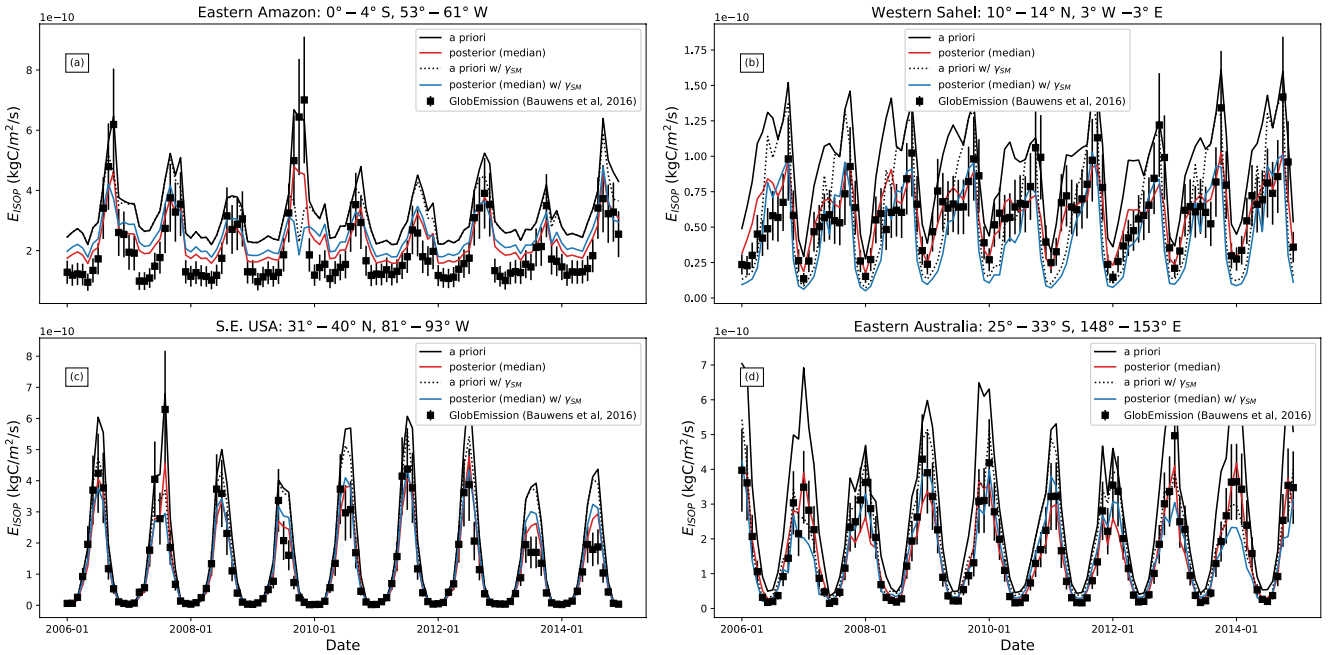

Figure 3. Comparison of a priori and posterior fluxes with top-down GlobEmission fluxes for (a) the eastern Amazon, (b) the western Sahel, (c) the southeastern US, and (d) eastern Australia. Shown are the a priori Model of Emissions of Gases and Aerosols from Nature (MEGAN2.1) fluxes (dashed-dotted line), the a priori fluxes with the inclusion of the MEGAN3 drought stress response γ_{SM} (dotted line), the median posterior MEGAN2.1 fluxes (solid red line), and the median posterior MEGAN2.1 fluxes with the inclusion of the MEGAN3 drought stress response γ_{SM} (solid blue line).

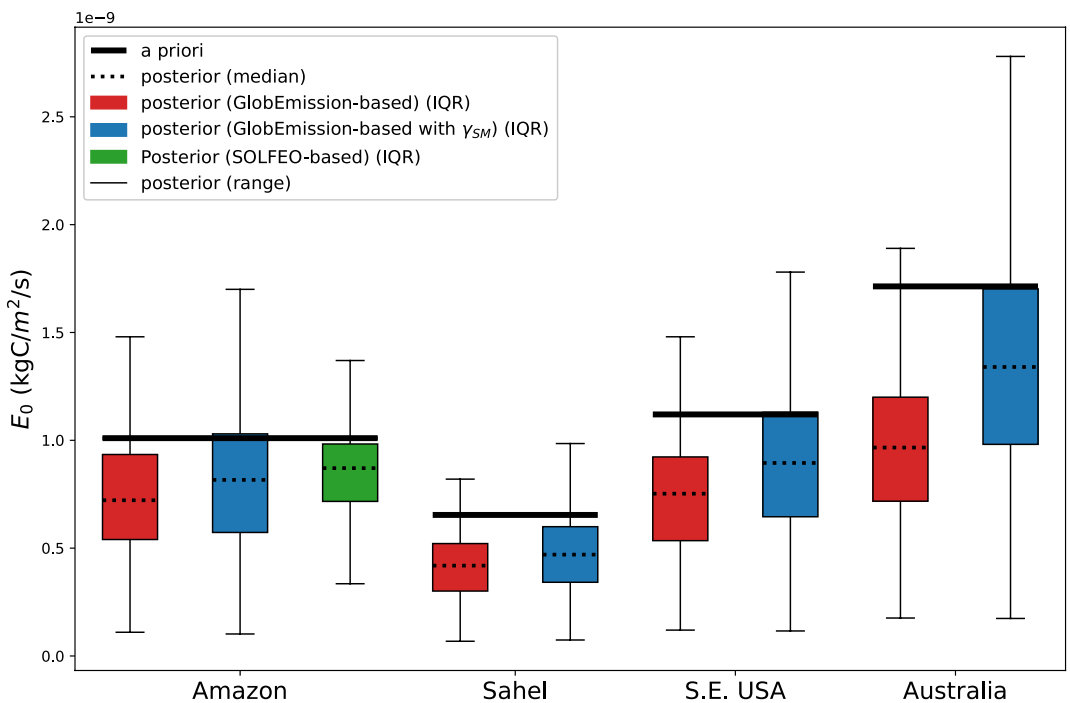

Figure 4. Comparison of the median posterior E_0 (dashed black lines) inferred from the top-down constraints in all four study regions. The colored boxes and error bars show the interquartile range and total range of the posterior E_0 distribution, respectively. The red boxes indicate the E_0 inferred from the OMI-based constraints and Model of Emissions of Gases and Aerosols from Nature (MEGAN2.1), whereas the blue boxes denote the E_0 estimated from the OMI-based constraints and MEGAN2.1 with the inclusion of the MEGAN3 drought stress response γ_{SM}. The green bar for the Amazon shows the posterior E_0 obtained from the TROPOspheric Monitoring Instrument-based SOLFEO fluxes.

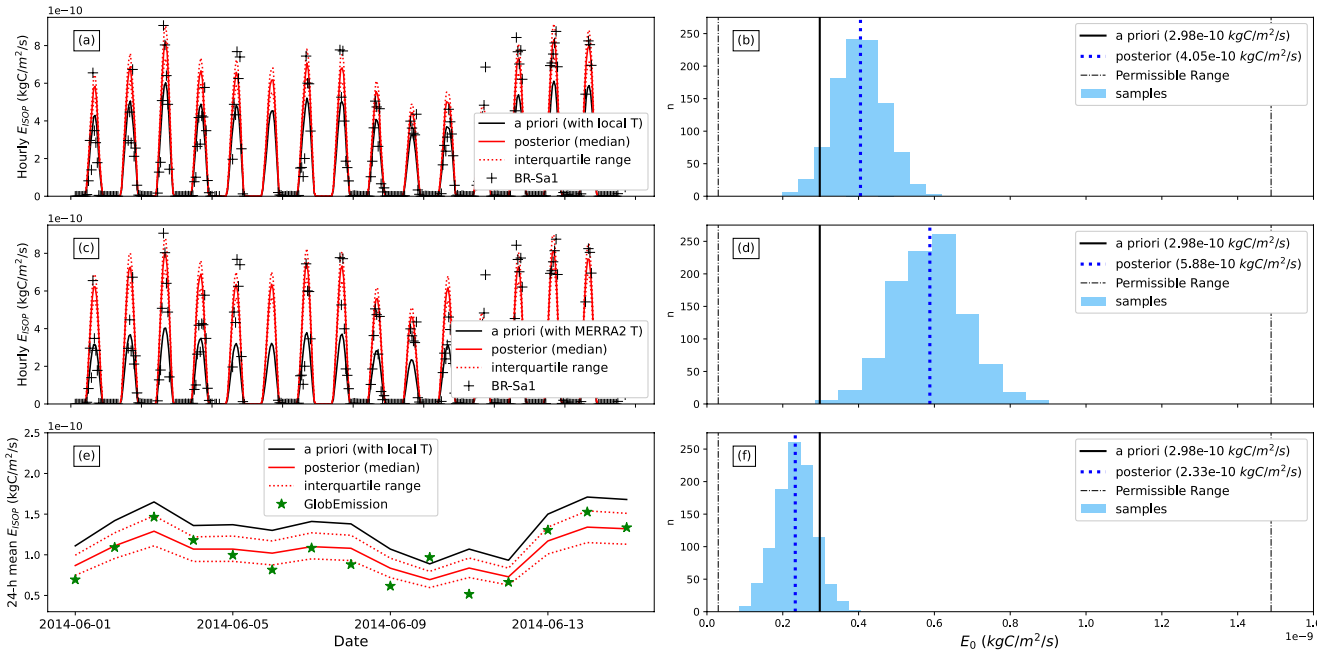

Figure 5. A priori and posterior isoprene fluxes and E_0 estimated with BR-Sa1 eddy covariance data (a–d) and GlobEmission fluxes (e–f). (a) Comparison of BR-Sa1 eddy covariance fluxes (+symbols) with a priori (black line) and posterior (red line) Model of Emissions of Gases and Aerosols from Nature (MEGAN) fluxes, estimated with local temperature data. (b) A priori E_0 and posterior distribution of E_0 calculated with local temperature data. (c) Comparison of BR-Sa1 eddy covariance fluxes (+symbols) with a priori (black line) and posterior (red line) MEGAN fluxes, calculated with Modern-Era Retrospective analysis for Research and Applications, Version 2 (MERRA-2) temperature data. (d) A priori E_0 and posterior distribution of E_0 inferred with MERRA-2 temperature data. (e) Comparison of GlobEmission isoprene fluxes (green stars) with 24-hr mean a priori (black line) and posterior (red line) MEGAN fluxes, estimated with local BR-Sa1 temperature data. (f) A priori E_0 and posterior distribution of E_0 inferred with local temperature data. The dotted red lines in panels (a, c, and e) denote the interquartile range. The dashed black vertical lines in (b, d, and f) denote the uniform a priori E_0 distribution, indicating the permissible range of E_0 values.

emissions are biased low relative to the BR-Sa1 observations, but this bias is largely corrected for in the optimization (Figure 5a). The posterior E_0 is well-constrained and approximately 36% larger than the a priori value (Figure 5b).

The optimization was highly sensitive to the temperature input data. Figure 5c shows that driving MEGAN with MERRA-2 temperatures leads to a significant reduction in the a priori emissions. This is due to the negative bias of the MERRA-2 temperature relative to the measured temperature at BR-Sa1 (approximately 1–2°K), which was also reported by Sarkar et al. (2020). The enhanced negative emission bias is compensated for by increasing the posterior E_0 by 45% relative to the local temperature case (Figure 5d). While the posterior emissions are similar in both cases (Figures 5a and 5c), the E_0 values which produce those emissions are very different. This is another example of equifinality, as described in Section 3.1.1. In this case, errors introduced by biases in the input temperature data are being compensated for in the optimization via a larger positive correction to E_0. This sensitivity to temperature, but also other model inputs like LAI and PAR, is a significant source of uncertainty which is discussed further in Section 4.2.

Optimizing MEGAN with daily top-down emissions from GlobEmission (Figure 5e) resulted in a 22% reduction in E_0 relative to the a priori (Figure 5f). This contrasts with the 36% increase in E_0 obtained using eddy covariance constraints in Figure 5b. The disagreement between these two optimization results reflects the discrepancies between the eddy covariance and top-down emissions, which have been previously reported in the Amazon (Gu et al., 2017). In Section 4.3 we discuss potential causes for these discrepancies, including biases in the OMI CH_2O columns (see Section 2.2.2), uncertainties in the chemical transport models that top-down emissions estimates rely on, and the representativeness of the eddy covariance flux measurements when compared to the larger spatial scales of the top-down emissions.

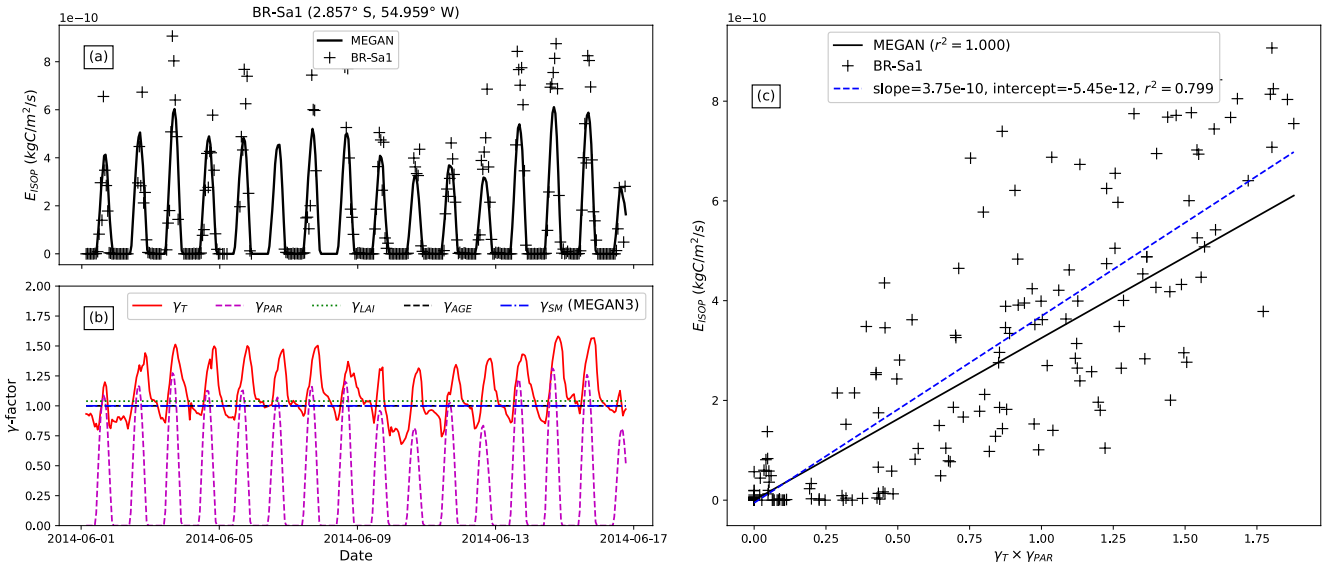

Figure 6. (a) Time series of BR-Sa1 (+symbols) and Model of Emissions of Gases and Aerosols from Nature (MEGAN) (solid black line) fluxes between 1 and 16 June 2014 (b) Time series of γ_T, γ_{PAR}, γ_{LAI}, γ_{AGE}, and γ_{SM} between 1 and 17 June 2014. (c) Correlation between the observed BR-Sa1 fluxes (+symbols) and the product $\gamma_T \times \gamma_{PAR}$ in MEGAN. The blue dashed line in (c) indicates the linear fit between the BR-Sa1 fluxes and $\gamma_T \times \gamma_{PAR}$, whereas the solid black line denotes the fit between the MEGAN fluxes and $\gamma_T \times \gamma_{PAR}$.

3.2. Optimization of Temperature Response γ_T

3.2.1. Tapajós National Forest (AmeriFlux Site BR-Sa1, Brazil)

Figure 6a shows the BR-Sa1 isoprene flux time series from 1 to 16 June 2014, along with the MEGAN a priori isoprene emissions calculated using locally measured temperature data (Sarkar et al., 2020). The time series of MEGAN γ factors plotted in Figure 6b shows that the variability in MEGAN is dominated by γ_T and γ_{PAR}, while γ_{LAI}, γ_{AGE}, and γ_{SM} have constant values at or very close to 1 throughout the time series. Figure 6c shows that both the modeled and observed emission variability is directly proportional to the temperature and sunlight response ($\gamma_T \times \gamma_{PAR}$), with a correlation of $r^2 = 0.799$ for the observed emissions. The steeper slope of the observed linear fit relative to MEGAN in Figure 6c is due to the large afternoon emission peaks observed in Figure 6a that are not apparent in the a priori emissions. The linear fit allows us to derive an observed temperature response γ'_T from the BR-Sa1 flux measurements.

The linear fit in Figure 6c gives

$$\gamma'_T = \frac{E_{ISOP} - b}{m\gamma_{PAR}}, \tag{8}$$

where E_{ISOP} is the observed isoprene emission rate, γ'_T is the observed temperature response, γ_{PAR} is the MEGAN sunlight response, and m and b are the slope and intercept of the linear fit, respectively. This is equivalent to solving Equation 1 for γ_T, with a slope of $m = E_0 \times C_{CE} \times \gamma_{LAI} \times \gamma_{AGE} \times \gamma_{CO_2} \times \gamma_{SM}$ and an intercept of $b = 0$. The strong correlation in Figure 6c indicate that the BR-Sa1 flux observations are broadly consistent with the diurnal variability in MEGAN which has been previously reported at this site (Sarkar et al., 2020), and the small value of the intercept b in Equation 8 is consistent with the functional form of MEGAN (Equation 1). A sensitivity test revealed that setting $b = 0$ had no measurable impact on γ'_T. To ensure a consistent methodology at both of our field sites, we retain the non-zero b value from Figure 6c in our subsequent analysis.

This derivation of γ'_T is sensitive to errors in model inputs and the other MEGAN γ factors. Uncertainties in E_0, γ_{LAI}, γ_{AGE}, and γ_{SM}, which are implicit in the slope m, are negligible as all four terms are constant for the BR-Sa1 time series. Constant errors in these terms would not impact the agreement between the MEGAN γ_T and observed γ'_T because both quantities would be scaled by the same constant slope m in Equation 8. Uncertainties in γ_{PAR} and in the PAR input data are important due to the large influence of γ_{PAR} on emission variability on short time scales, particularly given the lack of available local PAR measurements at BR-Sa1. We filtered the

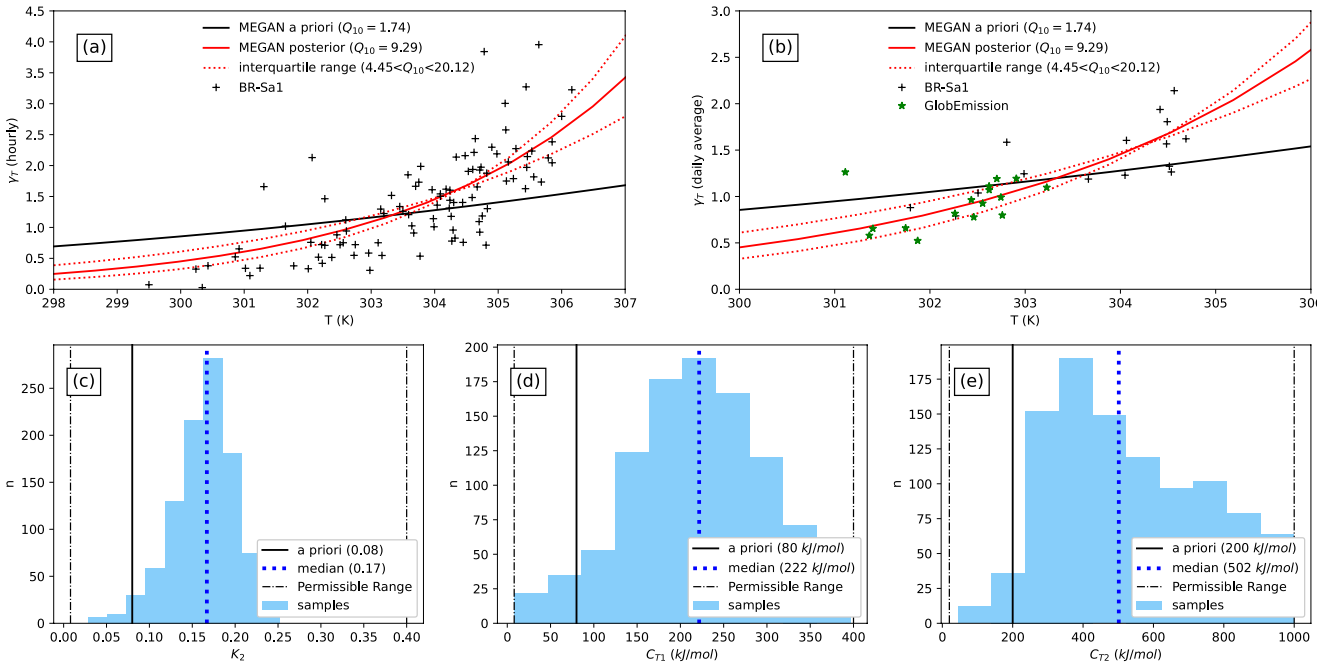

Figure 7. (a) A priori Model of Emissions of Gases and Aerosols from Nature (MEGAN) γ_T (black), median posterior γ_T (solid red) and interquartile range (dotted red) as a function of temperature (calculated using Equation 2) compared with the observed γ'_T (+symbols) at BR-Sa1 (calculated using Equation 8). (b) As in (a), but resampled from hourly to daily averages for comparison with OMI-based GlobEmission-derived temperature response (green stars). The Q_{10} values in (a and b) indicate the fractional change in γ_T between 303–313 K. Posterior parameter distributions for K_2, C_{T1}, and C_{T2} are shown in panels (c–e) (light blue). The median posterior values are indicated by the dashed blue lines in (c–e), while the a priori values are indicated by the solid black lines. The uniform a priori parameter distribution is indicated by the dashed black vertical line in panels (c–e).

observations for MERRA-2 PPFD >650 μmol/m^2/s (equivalent to PAR >136 W/m^2) to limit the impact of γ_{PAR} uncertainties on our calculation of γ'_T. This restricts our analysis to intervals centered around midday (approximately 10a.m.–4p.m. local time), limiting the variability of γ_{PAR} and preventing uncertainties in γ_{PAR} from being amplified under low-light conditions when the denominator in Equation 8 becomes small. Further increasing the PPFD threshold beyond 650 μmol/m^2/s did not significantly reduce scatter but led to excessive data loss. To avoid temperature-related uncertainties, only the locally measured temperature was used to drive MEGAN in the γ_T optimization.

The filtered γ'_T observations are shown in Figure 7a, along with the MEGAN a priori γ_T. The observed γ'_T is more sensitive to temperature compared to the a priori, which is consistent with the sharp afternoon emission peaks in the BR-Sa1 time series data that are not captured by MEGAN in Figure 6a.

MEGAN has different sensitivity to each of the γ_T parameters T_{Max}, K_1, K_2, C_{T1}, and C_{T2} (see Text S6 in Supporting Information S1). We therefore ran optimization experiments using all 31 unique combinations of these 5 parameters to identify the largest combination that could be reliably constrained by the observations while significantly improving model-observation agreement. The subset of K_2, C_{T1}, and C_{T2} yielded the best results, with the posterior γ_T agreeing closely with the observed γ'_T (Figure 7a). The posterior γ_T is more than 5 times more sensitive to temperature (Q_{10} = 9.29) than the a priori (Q_{10} = 1.74). This heightened temperature sensitivity is consistent with previous studies, which have found that the a priori MEGAN γ_T parameterization underestimates emissions at high temperatures for Australian *eucalypt* species (Emmerson et al., 2020) and Arctic vegetation (Angot et al., 2020; Kramshøj et al., 2016; Seco et al., 2020, 2022). Figure 7b shows that the median posterior γ_T is also consistent with the observed γ'_T as calculated with daily top-down GlobEmission fluxes, indicating that the top-down and eddy covariance constraints are consistent with respect to the temperature dependence of emissions. The K_2, C_{T1}, and C_{T2} distributions from the MHMCMC optimization are shown in Figures 7c–7e. All three parameters are well constrained and significantly different from the MEGAN a priori values (K_2: posterior = 0.17, prior = 0.08; C_{T1}: posterior = 222 kJ/mol, prior = 80 kJ/mol; C_{T2}: posterior = 502 kJ/mol, prior = 200 kJ/mol). Optimization of an alternative parameter combination is shown in Text S7 in Supporting Information S1.

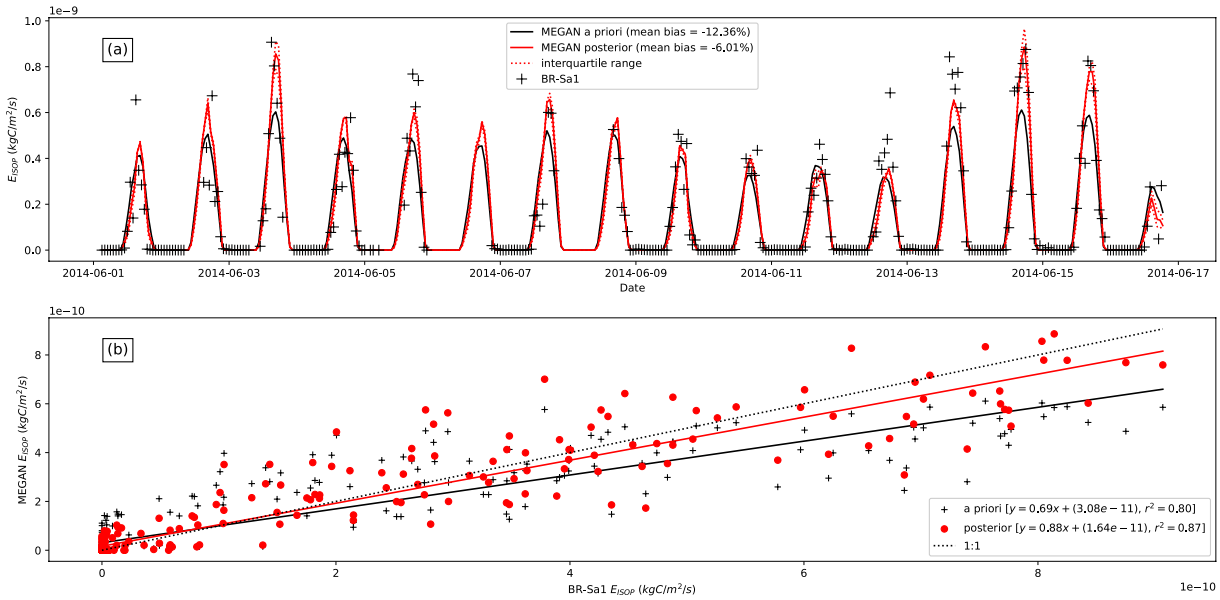

Figure 8. (a) A priori and posterior Model of Emissions of Gases and Aerosols from Nature (MEGAN) isoprene flux estimates at BR-Sa1 from 1 to 16 June 2014. The posterior emissions were calculated using the optimized γ_T based on eddy covariance observations (+symbols). The dotted red line denotes the interquartile range on the posterior emission estimate. The mean bias of the a priori and posterior MEGAN emissions relative to the BR-Sa1 measurements are indicated. (b) Correlation between observed and modeled hourly mean isoprene emission rates at BR-Sa1. The solid red line is a linear fit to the posterior modeled emissions (red circles), whereas the solid black curve is a linear fit to the a priori emissions (+symbols).

Figure 8a shows that the posterior MEGAN isoprene emissions are in good agreement with the BR-Sa1 measurements, with a mean bias reduction of ∼6% relative to the a priori. The temporal correlation between the modeled and observed emissions has also improved, with an r^2 value of 0.87 for the posterior emissions compared with 0.80 for the a priori emissions (Figure 8b). The improved correlation can also be seen in Figure 8a, where the posterior emissions are better able to capture the observed emissions peaks. This contrasts with the E_0 optimization at BR-Sa1 (Figure 5a). The slope (0.88 ± 0.02) and intercept ((1.64 ± 0.5)E−11) of the optimized γ_T regression in Figure 8b are significantly different from the regression of the optimized E_0 case (not shown; slope of 0.94 ± 0.03, intercept of (4.2 ± 0.8)E−11, and $r^2 = 0.80$).

3.2.2. Wytham Woods (WIsDOM Campaign, Oxford, UK)

Figure 9a shows the WIsDOM isoprene mixing ratio measurements from 25 May to 21 June 2018 at Wytham Woods (Ferracci, Bolas, et al., 2020, Ferracci, Harris, et al., 2020), resampled to hourly averages. Because the WIsDOM measurements are isoprene mixing ratios, a direct comparison with MEGAN is not possible without the use of an atmospheric model. However, an observed temperature response γ'_T can be obtained using the same methodology as at BR-Sa1 if the variability in the observed isoprene mixing ratios is primarily due to the temperature and sunlight emission response ($\gamma_T \times \gamma_{PAR}$). This requires that we filter the WIsDOM observations to minimize variability in photochemical loss rates and dispersion, the two main isoprene removal pathways (Ferracci, Bolas, et al., 2020). Of these two pathways, dispersion is the primary loss mechanism. Wytham Woods are approximately 0.5–1 km across, with the measurement site located in the middle. At the average daytime wind speed of ∼2–3 m/s during our measurement period, isoprene emitted at the edge of the woods would reach the measurement site in ∼4–8 min. There are no significant isoprene sources in the surrounding area, so the measurement footprint of this site is limited to Wytham Woods itself. The dispersion time scale is much shorter than the mean isoprene chemical lifetime of 30–60 min, based on modeled OH and O_3 from nearby monitoring stations (Ferracci, Bolas, et al., 2020).

Variability in photochemical loss rates was limited by filtering the WIsDOM observations for PPFD >850 μmol/m^2/s. This restricted our observations to mid-day (∼10a.m.–3p.m.) and also limited variability in the sunlight-driven isoprene emission response γ_{PAR}. Next, variability in horizontal dispersion rates (the primary isoprene loss mechanism at this site) was limited by retaining only those observations with a concurrent GEOS-FP 10-m windspeed within one standard deviation of the preheatwave mean (2.12–5.31 m s^{-1}). Variability in vertical

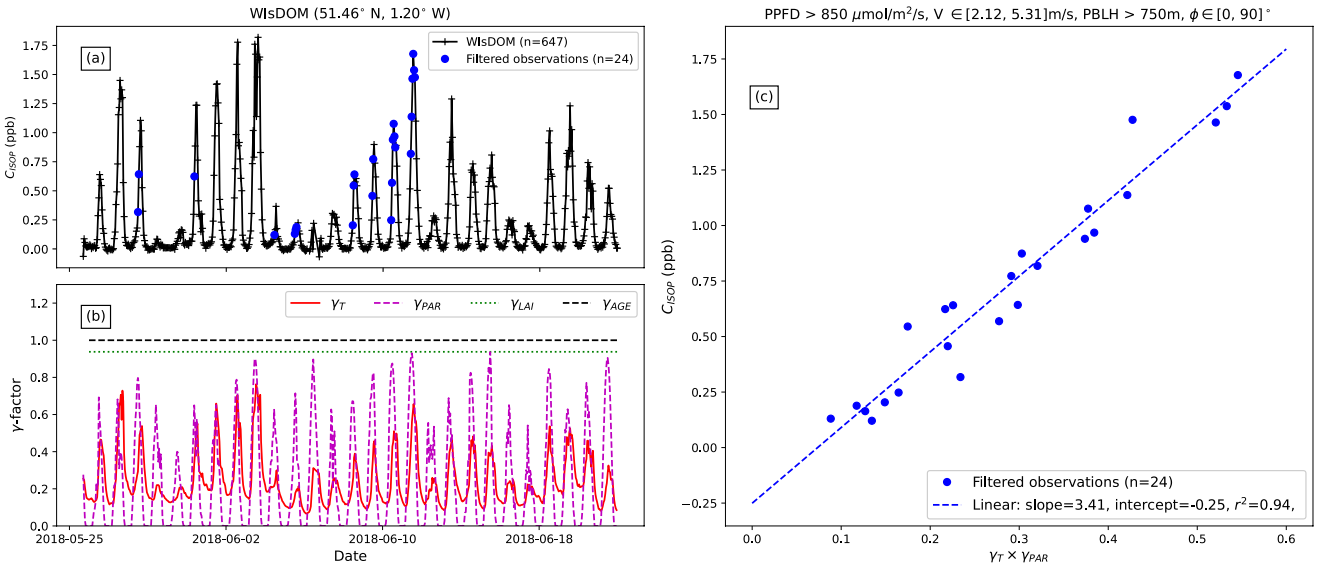

Figure 9. (a) Isoprene mixing ratios at the top of the canopy at Wytham Woods from 26 May to 21 June 2018 resampled to hourly averages. The blue circles indicate the observations which remain after filtering for PPFD >850 μmol/m^2/s, wind speed (V) between 2.12 m/s and 5.31 m/s, planetary boundary layer height >750 m, and wind direction (ϕ) between 0° and 90°. (b) Time series of a priori Model of Emissions of Gases and Aerosols from Nature (MEGAN) γ factors at Wytham Woods. (c) Correlation between the filtered Wytham Isoprene iDirac Oak Tree Measurements (WIsDOM) isoprene mixing ratio measurements (blue circles) and the product $\gamma_T \times \gamma_{PAR}$ in MEGAN. The blue dashed line in (c) indicates the linear fit between the filtered WIsDOM measurements and $\gamma_T \times \gamma_{PAR}$.

dispersion, though not a primary loss mechanism, is related to changes in the planetary boundary layer height (PBLH) and was reduced by filtering for GEOS-FP PBLH >750 m, as well as by our PPFD and windspeed filters due to the correlations between these variables. Finally, we filtered the remaining observations for northeasterly GEOS-FP winds (0–90°) because there are no other isoprene sources in this direction. These filtering steps ensured that the remaining isoprene measurements were directly proportional to the emission temperature and sunlight response $\gamma_T \times \gamma_{PAR}$, as shown by the linear fit in Figure 9c. Further details about the Wytham Woods measurement site and WIsDOM campaign are available in Ferracci, Bolas, et al. (2020).

The MEGAN γ factors for the preheatwave period at Wytham Woods are shown in Figure 9b. The MEGAN3 γ_{SM} was not available for 2018, but the insignificance of drought stress at Wytham Woods during the preheatwave period has been previously reported (Ferracci, Bolas, et al., 2020; Otu-Larbi et al., 2020). The leaf phenology activity factors γ_{LAI} and γ_{AGE} exhibited minimal variability (Ferracci, Bolas, et al., 2020). The variability of observed isoprene mixing ratios (Figure 9a) closely follows the variability of γ_T and γ_{PAR} (Figure 9b). This is confirmed in Figure 9c, which shows the strong linear correlation between the filtered Wytham Woods isoprene observations and $\gamma_T \times \gamma_{PAR}$. Following the same methodology as at BR-Sa1, we define an observed temperature response γ'_T as

$$\gamma'_T = \frac{C_{ISOP} - b}{m\gamma_{PAR}}, \tag{9}$$

where C_{ISOP} is the filtered isoprene mixing ratio, γ_{PAR} is the MEGAN sunlight response, and m and b are the slope and intercept of the linear fit in Figure 9c. In contrast to the Amazonian BR-Sa1 site (Equation 8), there is a non-zero intercept b in Equation 9. Because Equation 9 relates γ'_T to mixing ratios (C_{ISOP}) rather than emissions, we cannot assume that C_{ISOP} is directly proportional to the MEGAN γ factors over the full range of unfiltered observations and thus cannot impose an intercept of $b = 0$ without incurring additional uncertainty. Figure 10a shows that there is good agreement between the observed γ'_T and the a priori MEGAN γ_T, which is supported by the modeling work by Otu-Larbi et al. (2020) for the preheatwave period. This is in stark contrast to the behavior observed in Figure 7a at BR-Sa1.

The observed γ'_T was used to constrain the MEGAN γ_T parameters at Wytham Woods. We tested all 31 parameter combinations, but for consistency with BR-Sa1 we present only the optimization results for the subset K_2, C_{T1}, and C_{T2} (Figure 10). The posterior γ_T ($Q_{10} = 1.92$) is within error of the MEGAN a priori ($Q_{10} = 1.74$), and both

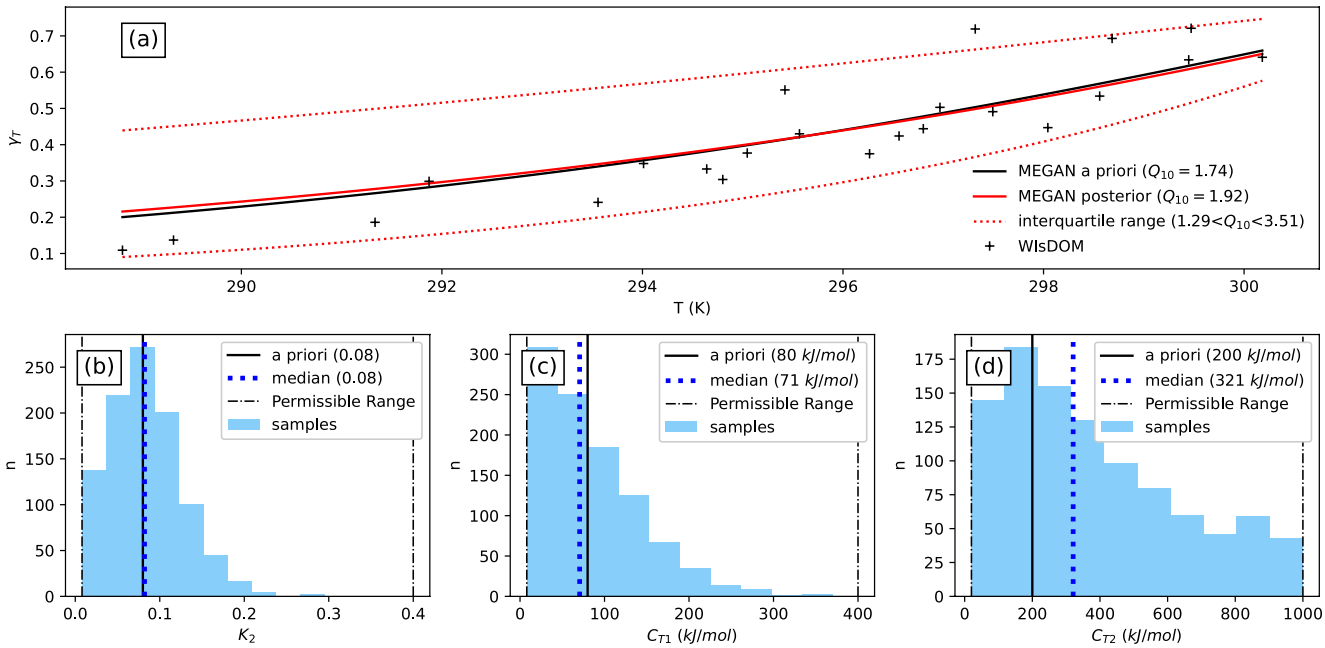

Figure 10. (a) A priori Model of Emissions of Gases and Aerosols from Nature (MEGAN) γ_T (black), median posterior γ_T (solid red) and interquartile range (dotted red) as a function of temperature (calculated using Equation 2) compared with the observed γ'_T (+symbols) (calculated using Equation 9 from filtered mixing ratio observations) at Wytham Woods. Posterior parameter distributions for K_2, C_{T1}, and C_{T2} are shown in panels (b–d) (light blue). The median posterior values are indicated by the dashed blue lines in (b–d), while the a priori values are indicated by the solid black lines. The uniform a priori parameter distribution is indicated by the dashed black vertical line in (b–d).

quantities are in good agreement with the observed γ'_T (Figure 10a). Figures (10b–10d) show that the γ_T parameters are not as precisely constrained as at BR-Sa1, which is due to the lower sensitivity of MEGAN to K_2 and C_{T1} at the lower ambient temperatures of Wytham Woods (see Text S6 in Supporting Information S1). Unlike at BR-Sa1 (Figures 8c–8e), the median posterior parameters are all relatively close to their a priori values. This indicates that the temperature sensitivity of isoprene emissions at Wytham Woods during the preheatwave period is accurately represented by the a priori parameterization of γ_T, in contrast to what was observed at BR-Sa1. This is discussed further in Section 4.4.

4. Discussion

Our experiments showed that the standard emission rate E_0 could be easily constrained with satellite-based top-down down emissions to reduce model biases. However, this optimization was very sensitive to drought stress and model input errors, and was found to be inconsistent with a ground-based E_0 optimization at our Amazonian BR-Sa1 field site. These sources of error are discussed in Section 4.1–4.3. We also found that γ_T could be constrained with ground-based observations, revealing an increased sensitivity of emissions to temperature at BR-Sa1. This result contrasted with our UK Wytham Woods site, where the a priori γ_T was in good agreement with the observations. We discuss the differences between these two field sites in Section 4.4.

4.1. Sensitivity to Drought Stress

The sensitivity of MEGAN to drought stress is a source of error in our parameter optimization experiments. Our optimization of E_0 in Eastern Australia was highly sensitive to the MEGAN3 drought stress activity factor γ_{SM} (Figure 3), consistent with previous studies (Emmerson et al., 2019). Enabling γ_{SM} increased the posterior E_0 by 40% relative to the no-γ_{SM} optimization because much of the bias between MEGAN and GlobEmission was already accounted for by the drought stress factor. We can mitigate this source of uncertainty by focusing our optimization efforts on regions and time periods which are not subject to drought stress, such as the Eastern Amazon during the BR-Sa1 measurement period and Wytham Woods during the 2018 preheatwave period.

While in principle we could enable the MEGAN3 γ_{SM} in all experiments to account for drought stress, there are uncertainties in γ_{SM} itself which limit the usefulness of such an approach. In particular, γ_{SM} does not account

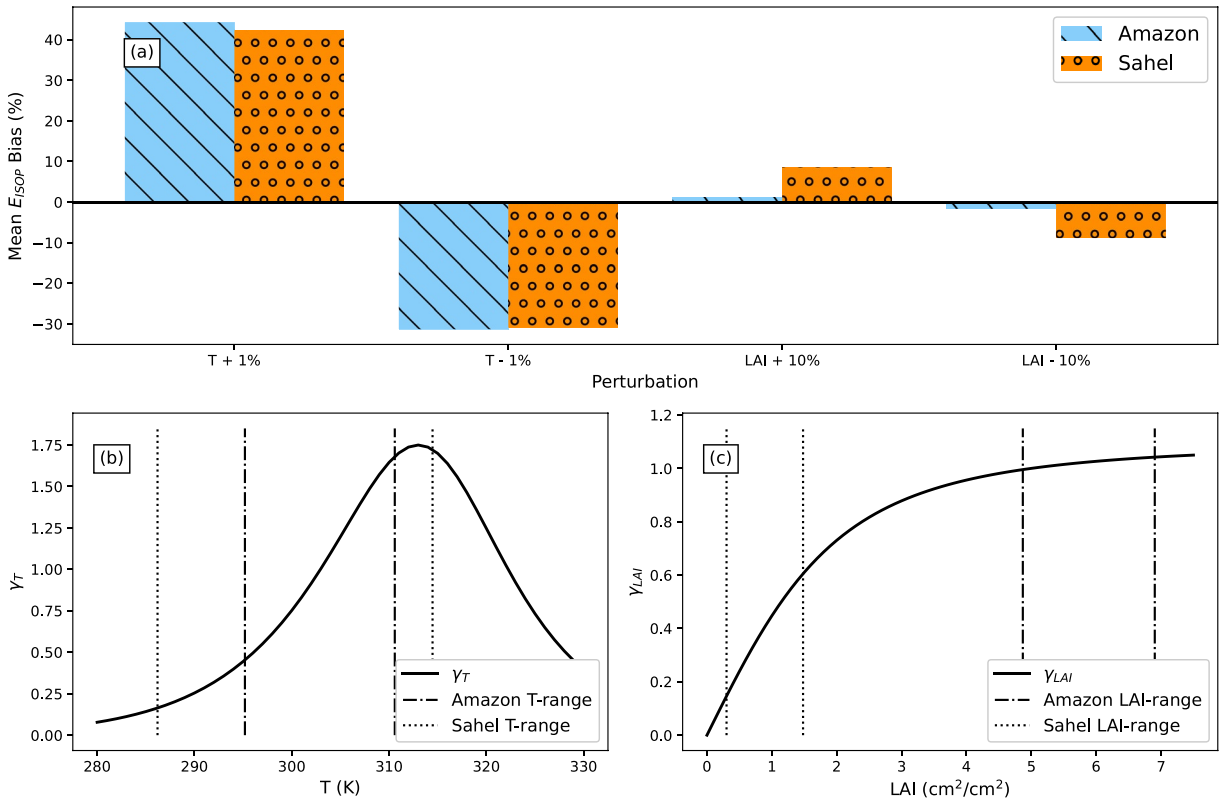

Figure 11. (a) Mean annual (2014) isoprene emission bias as calculated with Model of Emissions of Gases and Aerosols from Nature Version 2.1 (MEGANv2.1) in the Amazon (light blue) and the Sahel (orange) when running the model with biased temperature ($T \pm 1\%$) or leaf area index (LAI $\pm$ 10%) input data. (b) A priori MEGAN γ_T (calculated using Equation 2) superimposed with range of temperatures in the unperturbed Era Retrospective analysis for Research and Applications, Version 2 input data for both the Amazon (dash-dotted line) and the Sahel (dotted line) in 2014. (c) A priori MEGAN γ_{LAI} (calculated using Equation S5 in Supporting Information S1) superimposed with range of LAI values in the unperturbed 8-day average Moderate Resolution Imaging Spectroradiometer LAI input data for both the Amazon and the Sahel in 2014. The heightened sensitivity of MEGAN to LAI in the Sahel is indicated by the steeper slope of γ_{LAI} in the Sahel LAI range compared to the Amazon.

for the observed increase in isoprene emission rates that accompany moderate drought stress (Ferracci, Bolas, et al., 2020; Otu-Larbi et al., 2020; Potosnak et al., 2014; Saunier et al., 2020). Including γ_{SM} in our optimization experiments therefore risks misattributing uncertainties in γ_{SM} to other model parameters including E_0 and γ_T. A recent study has found that the parameterization of the MEGAN γ_{SM} can be improved using a combination of ecosystem-scale isoprene flux measurements and satellite-derived SM (Opacka et al., 2022). Future work in this direction, along with updates to the γ_{SM} algorithm to account for the impact of moderate drought stress on emissions, should improve the utility of the MEGAN drought stress response and allow parameter optimization experiments to be reliably performed under drought conditions.

4.2. Sensitivity to Errors in Model Input Data: Temperature and LAI

The sensitivity of MEGAN to meteorology and landcover inputs is another source of uncertainty in our parameter optimization. Biases in temperature and LAI inputs are particularly important, as these are among the primary drivers of short- and long-term variability in MEGAN, respectively (Alves et al., 2016, 2018; Chen et al., 2018; Guenther et al., 1993; Opacka et al., 2021). The impact of input biases on our optimization is apparent in Figures 5a–5d, where there is a 45% difference between the posterior E_0 at BR-Sa1 depending on whether local or MERRA-2 temperature data were used due to discrepancies between the two temperature data sets. These discrepancies could reflect region-specific biases in the MERRA-2 temperature data (e.g., Draper et al., 2018; Gupta et al., 2020) or could simply be due to the coarse spatial resolution of the MERRA-2 data.

The sensitivity of MEGAN isoprene emissions to temperature and LAI inputs is illustrated in Figure 11, which shows the impact of temperature and LAI biases on annual mean (2014) MEGAN isoprene emission rates in the Eastern Amazon and Western Sahel regions. A 1% temperature bias (~2.5–3.5 K, consistent with the difference between the local BR-Sa1 and MERRA-2 temperatures) leads to emission biases exceeding 30% (Figure 11a) in

both regions. This demonstrates the importance of using reliable air temperature measurements to drive MEGAN. However, even if the air temperature measurements are unbiased, the modeled isoprene emissions can still incur errors if the relationship between air temperature and leaf temperature is not parameterized properly in the model (see Section 4.4). This relationship is implicit in the parameterization of γ_T in our study but can also be modeled explicitly using full canopy physics models (e.g., Silva et al., 2020). Note that this sensitivity test used the a priori parameterization of γ_T ($Q_{10} = 1.74$). The impact of temperature input errors would be even more significant if we instead used the posterior parameterization from BR-Sa1 due to the enhanced temperature sensitivity of isoprene emissions at that site ($Q_{10} = 9.29$).

The sensitivity to LAI is much lower and varies significantly between the two regions, with a 10% LAI bias (based on the estimated uncertainty of the MODIS LAI product (Fang et al., 2013)) leading to a 10% emission bias in the Sahel but only a 2% emission bias in the Amazon (Figure 11a). This variable sensitivity is due to the saturation of γ_{LAI} in high-LAI environments such as the Amazon (Figure 11c), which represents the shading of foliage by the upper layers of the forest canopy (Guenther et al., 2006) (see Equation S5 in Text S8 in Supporting Information S1). Biases in LAI are therefore unlikely to have any significant impact on our optimization in high-LAI environments such as the Amazon but may introduce biases of 10% or more in low-LAI environments like the Sahel. In such cases, locally constrained LAI data may be necessary to mitigate this source of error and obtain reliable posterior parameters. The spatial variability of the MEGAN temperature and LAI sensitivity on a global scale is presented in Text S8 in Supporting Information S1.

Although the sensitivity to total LAI is low in the Amazon, measurements show that changes in the leaf-age fractionated LAI (i.e., the proportion of young, mature, or old leaves) can have a significant impact on Amazonian isoprene emissions (Alves et al., 2018; Wu et al., 2016). This effect is modeled by the leaf age activity factor γ_{AGE} (Guenther et al., 2006), but its influence is likely underestimated in the Amazon because the leaf age fractions are calculated based on changes in total LAI. Using directly measured leaf age fractions has been shown to improve MEGAN isoprene emissions in the Amazon basin (Alves et al., 2018). Given the short duration of the BR-Sa1 time series it is unlikely that γ_{AGE} would have a significant impact on our temperature optimization experiments, but it may introduce significant biases in our 9-year E_0 optimization based on top-down emissions.

Uncertainties in PAR input data are another potential source of error and may contribute to the E_0 biases seen in Section 3.1. However, these biases are likely smaller than the temperature-related biases shown in Figure 5c due to the lower sensitivity of MEGAN to PAR compared to temperature (Guenther et al., 2006). Time-dependent errors in PAR could impact our γ_T optimization, but this is largely accounted for by filtering out low-PAR observations at BR-Sa1 and Wytham Woods (see Section 3.2).

4.3. Discrepancies Between Top-Down and Eddy Covariance Constraints

The a priori MEGAN isoprene emissions at BR-Sa1 were biased high relative to the top-down constraints from GlobEmission (OMI-based) and SOLFEO (TROPOMI-based) but biased low relative to the local eddy covariance measurements, leading to inconsistent posterior E_0 values. The disagreement between the top-down and eddy covariance constraints is possibly due to the low bias of the OMI and TROPOMI CH_2O columns, discussed in Section 2.2.1. Note that similar discrepancies between top-down and eddy covariance isoprene fluxes have previously been reported in the Amazon (Gu et al., 2017), which may also have been due to underestimated spaceborne columns. Correcting the low OMI and TROPOMI CH_2O column biases with ground-based validation studies in the Amazon would result in higher top-down emissions than in GlobEmission and SOLFEO, and consequently smaller discrepancies between the top-down and eddy covariance constraints. Other uncertainties in top-down emissions may also contribute to these discrepancies. Top-down estimates are sensitive to CH_2O retrieval errors (Millet et al., 2006), chemistry-transport model errors (Barkley et al., 2013; Stavrakou et al., 2015), spatial smearing errors due to non-local CH_2O sources (Palmer et al., 2003; Turner et al., 2012), and non-biogenic CH_2O background sources such as biomass burning and methane oxidation (Marais et al., 2012; Wolfe et al., 2016).

Chemistry-transport model errors have been identified as a source of particular concern in top-down isoprene emissions in tropical regions due to their impacts on the CH_2O yield from isoprene oxidation as well as the diurnal variability of isoprene and CH_2O concentrations (Kefauver et al., 2014). This is relevant in the Amazon due to the large uncertainties in regional NO_2 and OH, both of which impact isoprene oxidation chemistry (Jeong et al., 2022; Liu et al., 2016, 2018; Wells et al., 2020; Wolfe et al., 2016). Stronger constraints on this chemistry,

such as direct space-based isoprene retrievals from the Cross-track Infrared Sounder (CrIS) (Fu et al., 2019; Wells et al., 2020), may mitigate some of these uncertainties. For example, CrIS isoprene column retrievals have recently been validated using ground-based remotely sensed isoprene columns in the Amazon and combined with OMI CH_2O and NO_2 retrievals to reveal large day-to-day variability in isoprene oxidation lifetime (Wells et al., 2022). Taking full advantage of top-down emissions estimates to optimize MEGAN will require a better understanding of the sensitivity of these estimates to chemistry-transport model errors. This sensitivity could be quantified by obtaining top-down emission estimates using multiple chemistry-transport models (Miyazaki et al., 2020). Simulated inversion experiments could also be performed to directly probe the impact of chemistry model errors on top-down emissions based on satellite pseudo-observations.

An additional important issue is the representativeness of the eddy covariance observations at BR-Sa1. The top-down fluxes are provided at $0.5° \times 0.5°$ spatial resolution, corresponding to a pixel size of roughly 3,000 km^2 near the equator (Bauwens et al., 2016). Extrapolating the BR-Sa1 flux measurements to this large pixel size can incur biases due to the spatial heterogeneity of isoprene emissions (Batista et al., 2019; Li et al., 2021). However, independent aircraft-based eddy covariance isoprene flux measurements from the Green Ocean Amazon campaign (Gu et al., 2017) show similar discrepancies with OMI-based emissions, which suggests that this problem cannot be entirely due to the representativeness of the BR-Sa1 measurements.

4.4. Variability of γ_T Between Ecosystems

The optimized $\boldsymbol{\gamma}_T$ at the Amazonian BR-Sa1 site was roughly five times more sensitive to temperature ($Q_{10} = 9.29$) than the MEGAN a priori ($Q_{10} = 1.74$). This could be due at least in part to the relationship between air temperature and leaf temperature. Isoprene emissions depend on leaf temperature, but MEGAN uses air temperature as an input. The relationship between these quantities is implicit in the PCEEA parameterization of γ_T, which was derived from canopy physics simulations for warm broadleaf forests and has been shown to introduce local emission biases of up to 25% relative to more sophisticated multi-level canopy model versions of MEGAN (Guenther et al., 2006). More sophisticated canopy models are also still subject to errors in the air-temperature/leaf-temperature relationship (e.g., Silva et al., 2020). It is therefore possible that errors in the parameterization of γ_T at BR-Sa1 reflect this underlying discrepancy between air temperature and leaf temperature. It is also possible that this is a physiological adaptation of the local vegetation to their high temperature environment, as was proposed by Emmerson et al. (2020) for the Australian *eucalypt* species from that study. However, without leaf-level temperature and isoprene flux measurements, we cannot disentangle any potential physiological effects from errors in the parameterization of the air-temperature/leaf-temperature relationship.

In any case, due to the increased temperature sensitivity of the posterior $\boldsymbol{\gamma}_T$, applying this parameterization to the broader Amazon region would have potentially significant impacts on regional isoprene emissions. However, it is difficult to extrapolate results from a single measurement site to a broader geographic area due to landcover and species distribution heterogeneity. Measurements from other Amazonian sites could be used to determine whether this posterior parameterization is representative of the region.

Unlike at BR-Sa1, the optimized $\boldsymbol{\gamma}_T$ at the UK Wytham Woods site was not significantly different from the a priori. This demonstrates that the performance of $\boldsymbol{\gamma}_T$ varies across ecosystems, and that any updates to the parameterization of $\boldsymbol{\gamma}_T$ should be applied on an ecosystem-specific scale. This has been done previously for Australian *eucalypt* species (Emmerson et al., 2020), and other studies have demonstrated that this may also be necessary for Arctic vegetation (Angot et al., 2020; Kramshøj et al., 2016; Seco et al., 2020, 2022). Accurately modeling the sensitivity of isoprene emissions to temperature will depend on the development of an ecosystem-specific parameterization for $\boldsymbol{\gamma}_T$, which could be derived using our methodology wherever suitable observations are available. This has the potential to significantly improve models of atmospheric chemistry in a warming climate or during severe heat wave events (Emmerson et al., 2020) in addition to improving day-to-day emission variability.

An unresolved source of uncertainty is the impact of drought stress on the emission temperature response. While the MEGAN a priori $\boldsymbol{\gamma}_T$ adequately describes the observed temperature response at Wytham Woods during the preheatwave period, increased temperature sensitivity was observed after the onset of a severe drought and heatwave in June 2018 (Ferracci, Bolas, et al., 2020; Otu-Larbi et al., 2020). A similar drought response was observed in an oak-dominated forest in the Missouri Ozarks (Seco et al., 2015). These observations are consistent with current conceptual models of the drought stress response, in which reduced transpiration of water through plant

leaves leads to an increase in leaf temperature and a stimulation of isoprene emissions (Potosnak et al., 2014). This shows that the temperature sensitivity of emissions is a function not only of ecosystem type but also of current environmental conditions including drought stress.

5. Summary and Conclusions

We have used Bayesian model-data fusion to optimize the standard emission rate and the temperature activity factor in MEGAN, using top-down isoprene fluxes derived from satellite observations in four regions (Amazon, Southeast USA, Western Sahel, and Eastern Australia), eddy covariance isoprene flux measurements in the Amazon, and isoprene atmospheric mixing ratio measurements in the United Kingdom.

Optimization of the standard emission rate E_0 with satellite constraints reduced model biases in the Amazon, the Southeast USA, the Western Sahel, and Eastern Australia. The optimized E_0 values were highly sensitive to model input errors. Sensitivity to temperature errors was extremely high in all regions, while sensitivity to total LAI errors was only significant in low-LAI environments such as the Western Sahel. The impact of the MEGAN3 drought stress response on the optimization was spatially and temporally variable, with the largest impact being seen in Eastern Australia. Uncertainties in the drought stress response are a major obstacle for reliable parameter optimization under drought conditions.

We optimized E_0 at the Amazonian BR-Sa1 field site using both satellite and eddy covariance constraints and found that the two results were inconsistent with one another. This mismatch may be largely due to the low biases identified in the satellite CH_2O retrievals used as constraints to derive the top-down emissions, leading to an underprediction of the top-down emission fluxes. Chemistry-transport model errors may add more uncertainty to the top-down emissions. Future optimization work using top-down emissions as constraints will be dependent on understanding and reducing the uncertainties in top-down emissions, which could be done through a combination of satellite validation studies with ground-based measurements and modeling studies to assess the impact of chemistry-transport model errors on top-down emissions. Stronger constraints could be placed on isoprene oxidation chemistry in models by combining satellite retrievals of CH_2O with retrievals of isoprene (e.g., Wells et al., 2020), while simultaneous optimization of isoprene and NO_X emissions may also improve top-down constraints due to the strong dependence of isoprene oxidation chemistry on ambient NO_X concentrations (Miyazaki et al., 2020).

Optimization of the temperature response γ_T with eddy covariance isoprene emission measurements increased the temperature sensitivity of the model by a factor of 5 (posterior $Q_{10} = 9.29$ compared to priori $Q_{10} = 1.74$) at BR-Sa1 and reduced model biases by 6%. By contrast, optimizing γ_T with isoprene mixing ratio measurements at the UK-based Wytham Woods site had no significant impact on the model parameters due to the good agreement between the MEGAN a priori γ_T and the observations. Enhanced sensitivity of isoprene emissions to temperature, and more specifically the underestimation of emissions at high temperatures, has now been observed in several ecosystem types, including an Amazonian old growth forest (this study), Australian *eucalpyt* trees (Emmerson et al., 2020), and various species of Arctic vegetation (Angot et al., 2020; Kramshøj et al., 2016; Seco et al., 2020, 2022). Drought stress has also been shown to increase temperature sensitivity at multiple temperate sites (Ferracci, Bolas, et al., 2020; Otu-Larbi et al., 2020; Seco et al., 2015). Accurate modeling of isoprene emissions, as well as their impacts on air quality and climate, will require an ecosystem-specific parameterization of the temperature emission response as well as an improved understanding of the drought stress emission response. Such a parameterization could be derived from ground-based isoprene and temperature measurements in a wide range of ecosystems. Existing measurements should be used to evaluate and reparametrize the temperature response where possible, while future measurement campaigns should target a wide range of ecosystem types. The use of longer measurement time series than presented in this paper would allow seasonal impacts such as drought to be investigated as well. The significance of isoprene emissions at high temperatures or under drought conditions is expected to increase in a warming climate (Emmerson et al., 2020; Saunier et al., 2020), further highlighting the need for a reliable parameterization of the emission temperature response.

Data Availability Statement

The MEGAN 2.1 source code (Guenther et al., 2012) and the MEGAN 3 drought stress activity factors (X. Jiang et al., 2018) can be obtained from https://bai.ess.uci.edu/megan/data-and-code. The MHMCMC Matlab code (Yang et al., 2021) is available at https://doi.org/10.5281/zenodo.4904195. The global OMI-based top-down

isoprene flux estimates (Bauwens et al., 2016) are available for download at https://emissions.aeronomie.be/index.php/omi-based/biogenic. The TROPOMI-based top-down isoprene flux estimates for South America are available for download at https://emissions.aeronomie.be/index.php/tropomi-based/isoprene-sa. The data from the WIsDOM campaign (Ferracci, Bolas et al., 2020, Ferracci, Harris et al., 2020) are available from the Natural Environment Research Council (NERC) Centre for Environmental Data Analysis (CEDA) archive at https://catalogue.ceda.ac.uk/uuid/0c39809848ce47bb850d8ca2045e40f2. The BR-Sa1 isoprene flux and temperature measurements (Sarkar et al., 2020, 2022) are available at https://bai.ess.uci.edu/research/data-archive. The MERRA-2 and GEOS-FP data used in this study have been provided by the Global Modeling and Assimilation Office (GMAO) at NASA Goddard Space Flight Center. The particular files used to drive MEGAN in this study were obtained from the GEOS-Chem (Bey et al., 2001) met-field archive at http://geoschemdata.wustl.edu. The MODIS 8-day LAI product (Yuan et al., 2011, 2020) is available at http://globalchange.bnu.edu.cn/research/laiv6.

Acknowledgments
C.A. DiMaria acknowledges a Canada Graduate Scholarship—Doctoral (CGS D) Grant funded by the Natural Sciences and Engineering Research Council of Canada (NSERC) (application no. PGSD3-546,721-2020). This work was also supported by Grant 16SUASEMIS from the Canadian Space Agency. R. Seco acknowledges a Ramón y Cajal Grant (RYC2020-029216-I) funded by MCIN/AEI/10.13039/501100011033 and by "ESF Investing in your future." IDAEA-CSIC is a Severo Ochoa Centre of Research Excellence (MCIN/AEI, Project CEX2018-000794-S). The BR-Sa1 field measurements were supported by Núcleo de Apoio à Pesquisa no Pará (NAPPA) em Santarém-Pa/Instituto Nacional de Pesquisas da Amazônia (INPA), Programa de Grande Escala Biosfera Atmosfera na Amazônia (LBA) and Instituto Chico Mendes de Conservação da Biodiversidade (ICMBio) em Santarém-Pa. V. Ferracci acknowledges funding from the Natural Environmental Research Council (NERC) project "Biodiversity and land-use impacts (BALI) on tropical ecosystems" (NE/K016377/1) in support of the Wytham Woods measurements. Part of this work was carried out at the Jet Propulsion Laboratory, California Institute of Technology, under a contract with the National Aeronautics and Space Administration (NASA).

References

Alves, E. G., Jardine, K., Tota, J., Jardine, A., Yãnez-Serrano, A. M., Karl, T., et al. (2016). Seasonality of isoprenoid emissions from a primary rainforest in central Amazonia. *Atmospheric Chemistry and Physics*, *16*(6), 3903–3925. https://doi.org/10.5194/acp-16-3903-2016

Alves, E. G., Tóta, J., Turnipseed, A., Guenther, A. B., Vega Bustillos, J. O., Santana, R. A., et al. (2018). Leaf phenology as one important driver of seasonal changes in isoprene emissions in Central Amazonia. *Biogeosciences*, *15*(13), 4019–4032. https://doi.org/10.5194/bg-15-4019-2018

Angot, H., McErlean, K., Hu, L., Millet, D. B., Hueber, J., Cui, K., et al. (2020). Biogenic volatile organic compound ambient mixing ratios and emission rates in the Alaskan Arctic tundra. *Biogeosciences*, *17*(23), 6219–6236. https://doi.org/10.5194/bg-17-6219-2020

Arneth, A., Schurgers, G., Lathiere, J., Duhl, T., Beerling, D. J., Hewitt, C. N., et al. (2011). Global terrestrial isoprene emission models: Sensitivity to variability in climate and vegetation. *Atmospheric Chemistry and Physics*, *11*(15), 8037–8052. https://doi.org/10.5194/acp-11-8037-2011

Ashworth, K., Wild, O., & Hewitt, C. N. (2010). Sensitivity of isoprene emissions estimated using MEGAN to the time resolution of input climate data. *Atmospheric Chemistry and Physics*, *10*(3), 1193–1201. https://doi.org/10.5194/acp-10-1193-2010

Barkley, M. P., Smedt, I. D., Van Roozendael, M., Kurosu, T. P., Chance, K., Arneth, A., et al. (2013). Top-down isoprene emissions over tropical South America inferred from SCIAMACHY and OMI formaldehyde columns. *Journal of Geophysical Research: Atmospheres*, *118*(12), 6849–6868. https://doi.org/10.1002/jgrd.50552

Batista, C. E., Ye, J., Ribeiro, I. O., Guimarães, P. C., Medeiros, A. S., Barbosa, R. G., et al. (2019). Intermediate-scale horizontal isoprene concentrations in the near-canopy forest atmosphere and implications for emission heterogeneity. *Proceedings of the National Academy of Sciences of the United States of America*, *116*(39), 19318–19323. https://doi.org/10.1073/pnas.1904154116

Bauwens, M., Stavrakou, T., Müller, J.-F., De Smedt, I., Van Roozendael, M., van der Werf, G. R., et al. (2016). Nine years of global hydrocarbon emissions based on source inversion of OMI formaldehyde observations. *Atmospheric Chemistry and Physics*, *16*(15), 10133–10158. https://doi.org/10.5194/acp-16-10133-2016

Bey, I., Jacob, D. J., Yantosca, R. M., Logan, J. A., Field, B. D., Fiore, A. M., et al. (2001). Global modeling of tropospheric chemistry with assimilated meteorology: Model description and evaluation. *Journal of Geophysical Research*, *106*(D19), 23073–23095. https://doi.org/10.1029/2001jd000807

Bloom, A. A., Bowman, K. W., Liu, J., Konings, A. G., Worden, J. R., Parazoo, N. C., et al. (2020). Lagged effects regulate the inter-annual variability of the tropical carbon balance. *Biogeosciences*, *17*(24), 6393–6422. https://doi.org/10.5194/bg-17-6393-2020

Bloom, A. A., & Williams, M. (2015). Constraining ecosystem carbon dynamics in a data-limited world: Integrating ecological "common sense" in a model–data fusion framework. *Biogeosciences*, *12*(5), 1299–1315. https://doi.org/10.5194/bg-12-1299-2015

Bloom, A. A., Worden, J., Jiang, Z., Worden, H., Kurosu, T., Frankenberg, C., & Schimel, D. (2015). Remote-sensing constraints on South America fire traits by Bayesian fusion of atmospheric and surface data. *Geophysical Research Letters*, *42*(4), 1268–1274. https://doi.org/10.1002/2014gl062584

Bolas, C. G., Ferracci, V., Robinson, A. D., Mead, M. I., Nadzir, M. S., Pyle, J. A., et al. (2020). iDIRAC: A field-portable instrument for long-term autonomous measurements of isoprene and selected VOCs. *Atmospheric Measurement Techniques*, *13*(2), 821–838. https://doi.org/10.5194/amt-13-821-2020

Buchholz, R. R., Worden, H. M., Park, M., Francis, G., Deeter, M. N., Edwards, D. P., et al. (2021). Air pollution trends measured from Terra: Co and AOD over industrial, fire-prone, and background regions. *Remote Sensing of Environment*, *256*, 112275. https://doi.org/10.1016/j.rse.2020.112275

Butt, N., Campbell, G., Malhi, Y., Morecroft, M., Fenn, K., & Thomas, M. (2009). *Initial results from establishment of a long-term broadleaf monitoring plot at Wytham Woods*. University of Oxford.

Chen, W. H., Guenther, A. B., Wang, X. M., Chen, Y. H., Gu, D. S., Chang, M., et al. (2018). Regional to global biogenic isoprene emission responses to changes in vegetation from 2000 to 2015. *Journal of Geophysical Research: Atmospheres*, *123*(7), 3757–3771. https://doi.org/10.1002/2017jd027934

Claeys, M., Graham, B., Vas, G., Wang, W., Vermeylen, R., Pashynska, V., et al. (2004). Formation of secondary organic aerosols through photooxidation of isoprene. *Science*, *303*(5661), 1173–1176. https://doi.org/10.1126/science.1092805

De Smedt, I., Pinardi, G., Vigouroux, C., Compernolle, S., Bais, A., Benavent, N., et al. (2021). Comparative assessment of TROPOMI and OMI formaldehyde observations and validation against MAX-DOAS network column measurements. *Atmospheric Chemistry and Physics*, *21*(16), 12561–12593. https://doi.org/10.5194/acp-21-12561-2021

De Smedt, I., Theys, N., Yu, H., Danckaert, T., Lerot, C., Compernolle, S., et al. (2018). Algorithm theoretical baseline for formaldehyde retrievals from S5P TROPOMI and from the QA4ECV project. *Atmospheric Measurement Techniques*, *11*(4), 2395–2426. https://doi.org/10.5194/amt-11-2395-2018

Draper, C. S., Reichle, R. H., & Koster, R. D. (2018). Assessment of MERRA-2 land surface energy flux estimates. *Journal of Climate*, *31*(2), 671–691. https://doi.org/10.1175/jcli-d-17-0121.1

Emmerson, K. M., Palmer, P. I., Thatcher, M., Haverd, V., & Guenther, A. B. (2019). Sensitivity of isoprene emissions to drought over south-eastern Australia: Integrating models and satellite observations of soil moisture. *Atmospheric Environment*, *209*, 112–124. https://doi.org/10.1016/j.atmosenv.2019.04.038

Emmerson, K. M., Possell, M., Aspinwall, M. J., Pfautsch, S., & Tjoelker, M. G. (2020). Temperature response measurements from eucalypts give insight into the impact of Australian isoprene emissions on air quality in 2050. *Atmospheric Chemistry and Physics*, *20*(10), 6193–6206. https://doi.org/10.5194/acp-20-6193-2020

Fang, H., Jiang, C., Li, W., Wei, S., Baret, F., Chen, J. M., et al. (2013). Characterization and intercomparison of global moderate resolution leaf area index (LAI) products: Analysis of climatologies and theoretical uncertainties. *Journal of Geophysical Research: Biogeosciences*, *118*(2), 529–548. https://doi.org/10.1002/jgrg.20051

Ferracci, V., Bolas, C. G., Freshwater, R. A., Staniaszek, Z., King, T., Jaars, K., et al. (2020). Continuous isoprene measurements in a UK temperate forest for a whole growing season: Effects of drought stress during the 2018 heatwave. *Geophysical Research Letters*, *47*(15), e2020GL088885. https://doi.org/10.1029/2020gl088885

Ferracci, V., Harris, N., Bolas, C., Jones, R., & Staniaszek, Z. (2020). Biodiversity and land use impacts on tropical forest ecosystem function (BALI): Isoprene concentration measurements at Wytham woods (UK) during the summer of 2018 [Dataset]. Centre for Environmental Data Analysis. https://catalogue.ceda.ac.uk/uuid/0c39809848ce47bb850d8ca2045e40f2

Filella, I., Zhang, C., Seco, R., Potosnak, M., Guenther, A., Karl, T., et al. (2018). A MODIS photochemical reflectance index (PRI) as an estimator of isoprene emissions in a temperate deciduous forest. *Remote Sensing*, *10*(4), 557. https://doi.org/10.3390/rs10040557

Fu, D., Millet, D. B., Wells, K. C., Payne, V. H., Yu, S., Guenther, A., & Eldering, A. (2019). Direct retrieval of isoprene from satellite-based infrared measurements. *Nature Communications*, *10*(1), 3811. https://doi.org/10.1038/s41467-019-11835-0

Gelaro, R., McCarty, W., Suárez, M. J., Todling, R., Molod, A., Takacs, L., et al. (2017). The modern-era retrospective analysis for research and applications, Version 2 (MERRA-2). *Journal of Climate*, *30*(14), 5419–5454. https://doi.org/10.1175/jcli-d-16-0758.1

Geron, C., Guenther, A., Sharkey, T., & Arnts, R. R. (2000). Temporal variability in basal isoprene emission factor. *Tree Physiology*, *20*(12), 799–805. https://doi.org/10.1093/treephys/20.12.799

Gu, D., Guenther, A. B., Shilling, J. E., Yu, H., Huang, M., Zhao, C., et al. (2017). Airborne observations reveal elevational gradient in tropical forest isoprene emissions. *Nature Communications*, *8*(1), 15541. https://doi.org/10.1038/ncomms15541

Guenther, A. B., Hewitt, C. N., Erickson, D., Fall, R., Geron, C., Graedel, T., et al. (1995). A global model of natural volatile organic compound emissions. *Journal of Geophysical Research*, *100*(D5), 8873–8892. https://doi.org/10.1029/94jd02950

Guenther, A. B., Karl, T., Harley, P., Wiedinmyer, C., Palmer, P. I., & Geron, C. (2006). Estimates of global terrestrial isoprene emissions using MEGAN (model of emissions of gases and aerosols from nature). *Atmospheric Chemistry and Physics*, *6*(11), 3181–3210. https://doi.org/10.5194/acp-6-3181-2006

Guenther, A. B., & Hills, A. J. (1998). Eddy covariance measurement of isoprene fluxes. *Journal of Geophysical Research*, *103*(D11), 13145–13152. https://doi.org/10.1029/97jd03283

Guenther, A. B., Jiang, X., Heald, C. L., Sakulyanontvittaya, T., Duhl, T., Emmons, L. K., & Wang, X. (2012). The model of emissions of gases and aerosols from nature Version 2.1 (MEGAN2.1): An extended and updated framework for modeling biogenic emissions. *Geoscientific Model Development*, *5*(6), 1471–1492. https://doi.org/10.5194/gmd-5-1471-2012

Guenther, A. B., Monson, R. K., & Fall, R. (1991). Isoprene and monoterpene emission rate variability: Observations with eucalyptus and emission rate algorithm development. *Journal of Geophysical Research*, *96*(D6), 10799. https://doi.org/10.1029/91jd00960

Guenther, A. B., Zimmerman, P. R., Harley, P. C., Monson, R. K., & Fall, R. (1993). Isoprene and monoterpene emission rate variability: Model evaluations and sensitivity analyses. *Journal of Geophysical Research*, *98*(D7), 12609–12617. https://doi.org/10.1029/93jd00527

Gupta, P., Verma, S., Bhatla, R., Chandel, A. S., Singh, J., & Payra, S. (2020). Validation of surface temperature derived from Merra-2 reanalysis against IMD gridded data set over India. *Earth and Space Science*, *7*(1), e2019EA000910. https://doi.org/10.1029/2019ea000910

Haario, H., Saksman, E., & Tamminen, J. (2001). An adaptive Metropolis algorithm. *Bernoulli*, *7*(2), 223. https://doi.org/10.2307/3318737

Hanson, D. T., & Sharkey, T. D. (2001). Rate of acclimation of the capacity for isoprene emission in response to light and temperature. *Plant, Cell and Environment*, *24*(9), 937–946. https://doi.org/10.1046/j.1365-3040.2001.00745.x

Heald, C., Wilkinson, M., Monson, R., Alo, C., Wang, G., & Guenther, A. (2009). Response of isoprene emission to ambient CO_2 changes and implications for global budgets. *Global Change Biology*, *15*(5), 1127–1140. https://doi.org/10.1111/j.1365-2486.2008.01802.x

Hudman, R. C., Murray, L. T., Jacob, D. J., Millet, D. B., Turquety, S., Wu, S., et al. (2008). Biogenic versus anthropogenic sources of CO in the United States. *Geophysical Research Letters*, *35*(4), L04801. https://doi.org/10.1029/2007gl032393

Jeong, D., Seco, R., Emmons, L., Schwantes, R., Liu, Y., McKinney, K. A., et al. (2022). Reconciling observed and predicted Tropical Rainforest oh concentrations. *Journal of Geophysical Research: Atmospheres*, *127*(1), e2020JD032901. https://doi.org/10.1029/2020jd032901

Jiang, X., Guenther, A., Potosnak, M., Geron, C., Seco, R., Karl, T., et al. (2018). Isoprene emission response to drought and the impact on global atmospheric chemistry. *Atmospheric Environment*, *183*, 69–83. https://doi.org/10.1016/j.atmosenv.2018.01.026

Jiang, Z., Worden, J. R., Worden, H., Deeter, M., Jones, D. B., Arellano, A. F., & Henze, D. K. (2017). A 15-year record of CO emissions constrained by MOPITT CO observations. *Atmospheric Chemistry and Physics*, *17*(7), 4565–4583. https://doi.org/10.5194/acp-17-4565-2017

Kaiser, J., Jacob, D. J., Zhu, L., Travis, K. R., Fisher, J. A., González Abad, G., et al. (2018). High-resolution inversion of OMI formaldehyde columns to quantify isoprene emission on ecosystem-relevant scales: Application to the southeast US. *Atmospheric Chemistry and Physics*, *18*(8), 5483–5497. https://doi.org/10.5194/acp-18-5483-2018

Karl, T., Apel, E., Hodzic, A., Riemer, D. D., Blake, D. R., & Wiedinmyer, C. (2009). Emissions of volatile organic compounds inferred from airborne flux measurements over a megacity. *Atmospheric Chemistry and Physics*, *9*(1), 271–285. https://doi.org/10.5194/acp-9-271-2009

Karl, T., Guenther, A., Yokelson, R. J., Greenberg, J., Potosnak, M., Blake, D. R., & Artaxo, P. (2007). The Tropical Forest and Fire Emissions Experiment: Emission, chemistry, and transport of biogenic volatile organic compounds in the lower atmosphere over Amazonia. *Journal of Geophysical Research*, *112*(D18), D18302. https://doi.org/10.1029/2007jd008539

Karl, T., Misztal, P. K., Jonsson, H. H., Shertz, S., Goldstein, A. H., & Guenther, A. B. (2013). Airborne flux measurements of BVOCs above Californian oak forests: Experimental investigation of surface and entrainment fluxes, oh densities, and Damköhler numbers. *Journal of the Atmospheric Sciences*, *70*(10), 3277–3287. https://doi.org/10.1175/jas-d-13-054.1

Kefauver, S. C., Filella, I., & Peñuelas, J. (2014). Remote sensing of atmospheric biogenic volatile organic compounds (BVOCs) via satellite-based formaldehyde vertical column assessments. *International Journal of Remote Sensing*, *35*(21), 7519–7542. https://doi.org/10.1080/01431161.2014.968690

Kramshøj, M., Vedel-Petersen, I., Schollert, M., Rinnan, Å., Nymand, J., Ro-Poulsen, H., & Rinnan, R. (2016). Large increases in arctic biogenic volatile emissions are a direct effect of warming. *Nature Geoscience*, *9*(5), 349–352. https://doi.org/10.1038/ngeo2692

Lawrence, D. M., Oleson, K. W., Flanner, M. G., Thornton, P. E., Swenson, S. C., Lawrence, P. J., et al. (2011). Parameterization improvements and functional and structural advances in Version 4 of the Community Land Model. *Journal of Advances in Modeling Earth Systems*, *3*(3), M03001. https://doi.org/10.1029/2011ms000045

Li, Y., Liu, B., Ye, J., Jia, T., Khuzestani, R. B., Sun, J. Y., et al. (2021). Unmanned aerial vehicle measurements of volatile organic compounds over a subtropical forest in China and implications for emission heterogeneity. *ACS Earth and Space Chemistry*, *5*(2), 247–256. https://doi.org/10.1021/acsearthspacechem.0c00271

Liu, Y., Brito, J., Dorris, M. R., Rivera-Rios, J. C., Seco, R., Bates, K. H., et al. (2016). Isoprene photochemistry over the amazon rainforest. *Proceedings of the National Academy of Sciences of the United States of America*, *113*(22), 6125–6130. https://doi.org/10.1073/pnas.1524136113

Liu, Y., Seco, R., Kim, S., Guenther, A. B., Goldstein, A. H., Keutsch, F. N., et al. (2018). Isoprene photo-oxidation products quantify the effect of pollution on hydroxyl radicals over Amazonia. *Science Advances*, *4*(4), eaar2547. https://doi.org/10.1126/sciadv.aar2547

Marais, E. A., Jacob, D. J., Guenther, A., Chance, K., Kurosu, T. P., Murphy, J. G., et al. (2014). Improved model of isoprene emissions in Africa using Ozone Monitoring Instrument (OMI) satellite observations of formaldehyde: Implications for oxidants and particulate matter. *Atmospheric Chemistry and Physics*, *14*(15), 7693–7703. https://doi.org/10.5194/acp-14-7693-2014

Marais, E. A., Jacob, D. J., Kurosu, T. P., Chance, K., Murphy, J. G., Reeves, C., et al. (2012). Isoprene emissions in Africa inferred from OMI observations of formaldehyde columns. *Atmospheric Chemistry and Physics*, *12*(14), 6219–6235. https://doi.org/10.5194/acp-12-6219-2012

Millet, D. B., Jacob, D. J., Turquety, S., Hudman, R. C., Wu, S., Fried, A., et al. (2006). Formaldehyde distribution over North America: Implications for satellite retrievals of formaldehyde columns and isoprene emission. *Journal of Geophysical Research*, *111*(D24), D24S02. https://doi.org/10.1029/2005jd006853

Misztal, P. K., Avise, J. C., Karl, T., Scott, K., Jonsson, H. H., Guenther, A. B., & Goldstein, A. H. (2016). Evaluation of regional isoprene emission factors and modeled fluxes in California. *Atmospheric Chemistry and Physics*, *16*(15), 9611–9628. https://doi.org/10.5194/acp-16-9611-2016

Misztal, P. K., Karl, T., Weber, R., Jonsson, H. H., Guenther, A. B., & Goldstein, A. H. (2014). Airborne flux measurements of biogenic isoprene over California. *Atmospheric Chemistry and Physics*, *14*(19), 10631–10647. https://doi.org/10.5194/acp-14-10631-2014

Miyazaki, K., Bowman, K. W., Yumimoto, K., Walker, T., & Sudo, K. (2020). Evaluation of a multi-model, multi-constituent assimilation framework for tropospheric chemical reanalysis. *Atmospheric Chemistry and Physics*, *20*(2), 931–967. https://doi.org/10.5194/acp-20-931-2020

Monson, R. K., Harley, P. C., Litvak, M. E., Wildermuth, M., Guenther, A. B., Zimmerman, P. R., & Fall, R. (1994). Environmental and developmental controls over the seasonal pattern of isoprene emission from Aspen leaves. *Oecologia*, *99*(3–4), 260–270. https://doi.org/10.1007/bf00627738

Monson, R. K., Weraduwage, S. M., Rosenkranz, M., Schnitzler, J.-P., & Sharkey, T. D. (2021). Leaf isoprene emission as a trait that mediates the growth-defense tradeoff in the face of climate stress. *Oecologia*, *197*(4), 885–902. https://doi.org/10.1007/s00442-020-04813-7

Mougin, E., Diawara, M. O., Soumaguel, N., Maïga, A. A., Demarez, V., Hiernaux, P., et al. (2019). A leaf area index data set acquired in Sahelian rangelands of Gourma in Mali over the 2005–2017 Period. *Earth System Science Data*, *11*(2), 675–686. https://doi.org/10.5194/essd-11-675-2019

Müller, J.-F., & Stavrakou, T. (2005). Inversion of CO and NOx emissions using the adjoint of the IMAGES model. *Atmospheric Chemistry and Physics*, *5*(5), 1157–1186. https://doi.org/10.5194/acp-5-1157-2005

Müller, J.-F., Stavrakou, T., & Peeters, J. (2019). Chemistry and deposition in the model of atmospheric composition at global and regional scales using inversion techniques for trace gas emissions (MAGRITTE v1.1)—Part 1: Chemical mechanism. *Geoscientific Model Development*, *12*(6), 2307–2356. https://doi.org/10.5194/gmd-12-2307-2019

Opacka, B., Müller, J.-F., Stavrakou, T., Bauwens, M., Sindelarova, K., Markova, J., & Guenther, A. B. (2021). Global and regional impacts of land cover changes on isoprene emissions derived from spaceborne data and the MEGAN model. *Atmospheric Chemistry and Physics*, *21*(11), 8413–8436. https://doi.org/10.5194/acp-21-8413-2021

Opacka, B., Müller, J.-F., Stavrakou, T., Miralles, D. G., Koppa, A., Pagán, B. R., et al. (2022). Impact of drought on isoprene fluxes assessed using field data, satellite-based gleam soil moisture and HCHO observations from OMI. *Remote Sensing*, *14*(9), 2021. https://doi.org/10.3390/rs14092021

Otu-Larbi, F., Bolas, C. G., Ferracci, V., Staniaszek, Z., Jones, R. L., Malhi, Y., et al. (2020). Modelling the effect of the 2018 summer heatwave and drought on isoprene emissions in a UK woodland. *Global Change Biology*, *26*(4), 2320–2335. https://doi.org/10.1111/gcb.14963

Palmer, P. I., Jacob, D. J., Fiore, A. M., Martin, R. V., Chance, K., & Kurosu, T. P. (2003). Mapping isoprene emissions over North America using formaldehyde column observations from space. *Journal of Geophysical Research*, *108*(D6), 4180. https://doi.org/10.1029/2002jd002153

Pétron, G., Harley, P., Greenberg, J., & Guenther, A. (2001). Seasonal temperature variations influence isoprene emission. *Geophysical Research Letters*, *28*(9), 1707–1710. https://doi.org/10.1029/2000gl011583

Potosnak, M. J., LeStourgeon, L., Pallardy, S. G., Hosman, K. P., Gu, L., Karl, T., et al. (2014). Observed and modeled ecosystem isoprene fluxes from an oak-dominated temperate forest and the influence of drought stress. *Atmospheric Environment*, *84*, 314–322. https://doi.org/10.1016/j.atmosenv.2013.11.055

Pugh, T. A. M., Ashworth, K., Wild, O., & Hewitt, C. N. (2013). Effects of the spatial resolution of climate data on estimates of biogenic isoprene emissions. *Atmospheric Environment*, *70*, 1–6. https://doi.org/10.1016/j.atmosenv.2013.01.001

Sarkar, C., Guenther, A. B., Park, J.-H., Seco, R., Alves, E., Batalha, S., et al. (2020). PTR-TOF-MS eddy covariance measurements of isoprene and monoterpene fluxes from an eastern Amazonian rainforest. *Atmospheric Chemistry and Physics*, *20*(12), 7179–7191. https://doi.org/10.5194/acp-20-7179-2020

Sarkar, C., Guenther, A. B., Park, J.-H., Seco, R., Alves, E., Batalha, S., et al. (2022). 2014 Tapajos Brazil PTRTOFMS isoprene fluxes [Dataset]. UCI BAI—Data Archive. Retrieved, from https://bai.ess.uci.edu/research/data-archive

Saunier, A., Ormeño, E., Piga, D., Armengaud, A., Boissard, C., Lathière, J., et al. (2020). Isoprene contribution to ozone production under climate change conditions in the French Mediterranean Area. *Regional Environmental Change*, *20*(4), 111. https://doi.org/10.1007/s10113-020-01697-4

Seco, R., Holst, T., Davie-Martin, C. L., Simin, T., Guenther, A., Pirk, N., et al. (2022). Strong isoprene emission response to temperature in tundra vegetation. *Proceedings of the National Academy of Sciences of the United State of America*, *119*(38), e2118014119. https://doi.org/10.1073/pnas.2118014119

Seco, R., Holst, T., Matzen, M. S., Westergaard-Nielsen, A., Li, T., Simin, T., et al. (2020). Volatile organic compound fluxes in a subarctic peatland and lake. *Atmospheric Chemistry and Physics*, *20*(21), 13399–13416. https://doi.org/10.5194/acp-20-13399-2020

Seco, R., Karl, T., Guenther, A., Hosman, K. P., Pallardy, S. G., Gu, L., et al. (2015). Ecosystem-scale volatile organic compound fluxes during an extreme drought in a broadleaf temperate forest of the Missouri Ozarks (central USA). *Global Change Biology*, *21*(10), 3657–3674. https://doi.org/10.1111/gcb.12980

Silva, S. J., Heald, C. L., & Guenther, A. B. (2020). Development of a reduced-complexity plant canopy physics surrogate model for use in chemical transport models: A case study with GEOS-Chem V12.3.0. *Geoscientific Model Development*, *13*(6), 2569–2585. https://doi.org/10.5194/gmd-13-2569-2020

Situ, S., Wang, X., Guenther, A., Zhang, Y., Wang, X., Huang, M., et al. (2014). Uncertainties of isoprene emissions in the MEGAN model estimated for a coniferous and broad-leaved mixed forest in southern China. *Atmospheric Environment*, *98*, 105–110. https://doi.org/10.1016/j.atmosenv.2014.08.023

Sprengnether, M., Demerjian, K. L., Donahue, N. M., & Anderson, J. G. (2002). Product analysis of the OH oxidation of isoprene and 1,3-butadiene in the presence of NO. *Journal of Geophysical Research*, *107*(D15), 4268. https://doi.org/10.1029/2001jd000716

Stavrakou, T., Müller, J.-F., Bauwens, M., De Smedt, I., Lerot, C., Van Roozendael, M., et al. (2016). Substantial underestimation of post-harvest burning emissions in the North China Plain revealed by multi-species space observations. *Scientific Reports*, *6*(1), 32307. https://doi.org/10.1038/srep32307

Stavrakou, T., Müller, J.-F., Bauwens, M., De Smedt, I., Van Roozendael, M., De Mazière, M., et al. (2015). How consistent are top-down hydrocarbon emissions based on formaldehyde observations from GOME-2 and OMI? *Atmospheric Chemistry and Physics*, *15*(20), 11861–11884. https://doi.org/10.5194/acp-15-11861-2015

Stavrakou, T., Müller, J.-F., De Smedt, I., Van Roozendael, M., Kanakidou, M., Vrekoussis, M., et al. (2009a). The continental source of glyoxal estimated by the synergistic use of spaceborne measurements and inverse modelling. *Atmospheric Chemistry and Physics*, *9*(21), 8431–8446. https://doi.org/10.5194/acp-9-8431-2009

Stavrakou, T., Müller, J.-F., De Smedt, I., Van Roozendael, M., van der Werf, G. R., Giglio, L., & Guenther, A. (2009b). Evaluating the performance of pyrogenic and biogenic emission inventories against one decade of space-based formaldehyde columns. *Atmospheric Chemistry and Physics*, *9*(3), 1037–1060. https://doi.org/10.5194/acp-9-1037-2009

Stavrakou, T., Müller, J.-F., De Smedt, I., Van Roozendael, M., van der Werf, G. R., Giglio, L., & Guenther, A. (2009c). Global emissions of non-methane hydrocarbons deduced from SCIAMACHY formaldehyde columns through 2003–2006. *Atmospheric Chemistry and Physics*, *9*(11), 3663–3679. https://doi.org/10.5194/acp-9-3663-2009

Trainer, M., Williams, E. J., Parrish, D. D., Buhr, M. P., Allwine, E. J., Westberg, H. H., et al. (1987). Models and observations of the impact of natural hydrocarbons on rural ozone. *Nature*, *329*(6141), 705–707. https://doi.org/10.1038/329705a0

Turner, A. J., Henze, D. K., Martin, R. V., & Hakami, A. (2012). The spatial extent of source influences on modeled column concentrations of short-lived species. *Geophysical Research Letters*, *39*(12). https://doi.org/10.1029/2012gl051832

Vigouroux, C., Langerock, B., Bauer Aquino, C. A., Blumenstock, T., Cheng, Z., De Mazière, M., et al. (2020). Tropomi–sentinel-5 precursor formaldehyde validation using an extensive network of ground-based Fourier-transform infrared stations. *Atmospheric Measurement Techniques*, *13*(7), 3751–3767. https://doi.org/10.5194/amt-13-3751-2020

Wells, K. C., Millet, D. B., Payne, V. H., Deventer, M. J., Bates, K. H., de Gouw, J. A., et al. (2020). Satellite isoprene retrievals constrain emissions and atmospheric oxidation. *Nature*, *585*(7824), 225–233. https://doi.org/10.1038/s41586-020-2664-3

Wells, K. C., Millet, D. B., Payne, V. H., Vigouroux, C., Aquino, C. A., De Mazière, M., et al. (2022). Next-generation isoprene measurements from space: Detecting daily variability at high resolution. *Journal of Geophysical Research: Atmospheres*, *127*(5), e2021JD036181. https://doi.org/10.1029/2021jd036181

Wiedinmyer, C., Greenberg, J., Guenther, A., Hopkins, B., Baker, K., Geron, C., et al. (2005). Ozarks Isoprene Experiment (OZIE): Measurements and modeling of the "isoprene volcano". *Journal of Geophysical Research*, *110*(D18), D18307. https://doi.org/10.1029/2005jd005800

Wolfe, G. M., Kaiser, J., Hanisco, T. F., Keutsch, F. N., de Gouw, J. A., Gilman, J. B., et al. (2016). Formaldehyde production from isoprene oxidation across NOx regimes. *Atmospheric Chemistry and Physics*, *16*(4), 2597–2610. https://doi.org/10.5194/acp-16-2597-2016

Worden, H. M., Bloom, A. A., Worden, J. R., Jiang, Z., Marais, E. A., Stavrakou, T., et al. (2019). New constraints on biogenic emissions using satellite-based estimates of carbon monoxide fluxes. *Atmospheric Chemistry and Physics*, *19*(21), 13569–13579. https://doi.org/10.5194/acp-19-13569-2019

Worden, H. M., Deeter, M. N., Frankenberg, C., George, M., Nichitiu, F., Worden, J., et al. (2013). Decadal record of satellite carbon monoxide observations. *Atmospheric Chemistry and Physics*, *13*(2), 837–850. https://doi.org/10.5194/acp-13-837-2013

Wu, J., Albert, L. P., Lopes, A. P., Restrepo-Coupe, N., Hayek, M., Wiedemann, K. T., et al. (2016). Leaf development and demography explain photosynthetic seasonality in Amazon evergreen forests. *Science*, *351*(6276), 972–976. https://doi.org/10.1126/science.aad5068

Xu, T., White, L., Hui, D., & Luo, Y. (2006). Probabilistic inversion of a terrestrial ecosystem model: Analysis of uncertainty in parameter estimation and model prediction. *Global Biogeochemical Cycles*, *20*(2), GB2007. https://doi.org/10.1029/2005gb002468

Yang, Y., Bloom, A. A., Ma, S., Levine, P., Norton, A., Parazoo, N. C., et al. (2021). CARDAMOM-FluxVal version 1.0 [Software]. Zenodo. https://doi.org/10.5281/zenodo.4904195

Yang, Y., Bloom, A. A., Ma, S., Levine, P., Norton, A., Parazoo, N. C., et al. (2022). CARDAMOM-FluxVal version 1.0: A FLUXNET-based validation system for cardamom carbon and water flux estimates. *Geoscientific Model Development*, *15*(4), 1789–1802. https://doi.org/10.5194/gmd-15-1789-2022

Yu, H., Guenther, A., Gu, D., Warneke, C., Geron, C., Goldstein, A., et al. (2017). Airborne measurements of isoprene and monoterpene emissions from Southeastern U.S. forests. *Science of the Total Environment*, *595*, 149–158. https://doi.org/10.1016/j.scitotenv.2017.03.262

Yuan, H., Dai, Y., & Li, S. (2020). *Reprocessed MODIS Version 6 Leaf Area Index data sets for land surface and climate modelling* [Dataset]. Sun Yat-sun University. Retrieved from http://globalchange.bnu.edu.cn/research/laiv6#cite

Yuan, H., Dai, Y., Xiao, Z., Ji, D., & Shangguan, W. (2011). Reprocessing the MODIS Leaf Area Index products for land surface and climate modelling. *Remote Sensing of Environment*, *115*(5), 1171–1187. https://doi.org/10.1016/j.rse.2011.01.001

Ziehn, T., Scholze, M., & Knorr, W. (2012). On the capability of Monte Carlo and adjoint inversion techniques to derive posterior parameter uncertainties in terrestrial ecosystem models. *Global Biogeochemical Cycles*, *26*(3), GB3025. https://doi.org/10.1029/2011gb004185